Combustion and Flame 158 (2011) 1491–1506

Contents lists available at ScienceDirect

Combustion and Flame

journal homepage: www.elsevier.com/locate/combustflame

Homogeneous combustion of fuel-lean $H_2/O_2/N_2$ mixtures over platinum at elevated pressures and preheats

Yohannes Ghermay [a], John Mantzaras [a,*], Rolf Bombach [a], Konstantinos Boulouchos [b]

[a] Paul Scherrer Institute, Combustion Research, CH-5232 Villigen PSI, Switzerland
[b] Swiss Federal Institute of Technology, Laboratory of Aerothermochemistry and Combustion Systems, CH-8092 Zurich, Switzerland

ARTICLE INFO

Article history:
Received 19 October 2010
Received in revised form 8 December 2010
Accepted 21 December 2010
Available online 20 January 2011

Keywords:
Homogeneous combustion of hydrogen over platinum
High pressure and high preheat combustion of hydrogen
In situ Raman and LIF measurements
Channel flow combustion

ABSTRACT

The gas-phase combustion of $H_2/O_2/N_2$ mixtures over platinum was investigated experimentally and numerically at fuel-lean equivalence ratios up to 0.30, pressures up to 15 bar and preheats up to 790 K. In situ 1-D spontaneous Raman measurements of major species concentrations and 2-D laser induced fluorescence (LIF) of the OH radical were applied in an optically accessible channel-flow catalytic reactor, leading to the assessment of the underlying heterogeneous (catalytic) and homogeneous (gas-phase) combustion processes. Simulations were carried out with a 2-D elliptic code that included elementary hetero-/homogeneous chemical reaction schemes and detailed transport. Measurements and predictions have shown that as pressure increased above 10 bar the preheat requirements for significant gas-phase hydrogen conversion raised appreciably, and for $p = 15$ bar (a pressure relevant for gas turbines) even the highest investigated preheats were inadequate to initiate considerable gas-phase conversion. Simulations in channels with practical geometrical confinements of 1 mm indicated that gas-phase combustion was altogether suppressed at atmospheric pressure, wall temperatures as high as 1350 K and preheats up to 773 K. While homogeneous ignition chemistry controlled gaseous combustion at atmospheric pressure, flame propagation characteristics dictated the strength of homogeneous combustion at the highest investigated pressures. The decrease in laminar burning rates for $p \geqslant 8$ bar led to a push of the gaseous reaction zone close to the channel wall, to a subsequent leakage of hydrogen through the gaseous reaction zone, and finally to catalytic conversion of the escaped fuel at the channel walls. Parametric studies delineated the operating conditions and geometrical confinements under which gas-phase conversion of hydrogen could not be ignored in numerical modeling of catalytic combustion.

1. Introduction

In recent years, there has been a growing interest in hydrogen and hydrogen-rich fuel combustion for large-scale power plants and also for microreactors of portable power generation systems. In the former application, hydrogen-rich gases can be produced by decarbonization of fossil fuels, eventually leading to precombustion capture of CO_2 [1]. Hydrogen-containing fuels are also of interest for new postcombustion CO_2 capture strategies in natural-gas-fired power plants, wherein the fuel/air mixture is diluted with large exhaust gas recycle in order to increase the content of CO_2 in the flue gases and thus facilitate its subsequent capture [2]. In this case, hydrogen produced via reforming a fraction of the natural gas can be added to the main fuel stream in order to increase the combustion stability of the highly diluted reactive mixture [2,3]. Hydrogen fuels are finally of interest in microreactors used for small-scale ($\sim$100 W_e) power generation [4,5]. Therein, hydrogen can be produced from methane [6–8] or higher hydrocarbons [9–11] in suitable catalytic microreformers.

Even though lean premixed combustion constitutes the mainstream approach in gas-fired power plants, hybrid methodologies involving catalytic (heterogeneous) and gas-phase (homogeneous) combustion are intensively investigated in the last years as a means to reduce NO_x emissions and improve combustion stability [12]. In one such hybrid concept, part of the fuel is converted catalytically in a honeycomb reactor and the remaining is combusted in a follow-up homogeneous burner [12], with both combustion modules operating at fuel-lean stoichiometries. While combined hetero-/homogeneous combustion is an option for the aforementioned combustion technologies in large-scale power generation, it is the preferred method for microreactors. Prime reasons for this choice are the large surface-to-volume ratios of microreactors that favor catalytic surface conversion over volumetric gaseous combustion, the occurrence of many undesirable flame instabilities at small geometrical confinements driven by flame–wall interactions [13–16], and the efficient suppression of such instabilities by coating the reactor walls with an active catalyst [17,18].

* Corresponding author. Fax: +41 56 3102199.
E-mail address: ioannis.mantzaras@psi.ch (J. Mantzaras).

0010-2180/$ - see front matter © 2010 The Combustion Institute. Published by Elsevier Inc. All rights reserved.
doi:10.1016/j.combustflame.2010.12.025

Nomenclature

b	channel half-height, Fig. 1
$c_{p,k}$	specific heat at constant pressure of kth gaseous species, Eq. (7)
d	channel diameter
D_{km}	mixture-average species diffusion coefficient, Eq. (6)
D_k^T	species thermal diffusion coefficient, Eq. (6)
h, h_k^o	total enthalpy, chemical enthalpy of the kth gaseous species, Eq. (3)
$\underline{\underline{I}}$	unity diagonal matrix, Eq. (2)
K_g	total number of gaseous species, Eq. (4)
L	catalytic reactor length, Fig. 1
Le	Lewis number (thermal over mass diffusivity)
$\dot{m}, \dot{M}$	mass flux, mass flow rate
M_s	total number of surface species, Eq. (5)
p	pressure
r	radial coordinate
R^o	universal gas constant, Eq. (7)
Re_{IN}	inlet Reynolds number
$\dot{s}_k$	catalytic molar production rate of kth species, Eq. (8)
S_L	laminar flame speed, Fig. 12
T	temperature
T_o	fresh mixture temperature, Fig. 12, and reference temperature, Eq. (7)
u, U_{IN}	streamwise velocity component, inlet streamwise velocity
v	transverse ($-y$) or radial ($-r$) velocity component
$\vec{V}_k$	species diffusion velocity vector, Eq. (6)
W	catalytic channel width, Fig. 1
W_k, $\overline{W}$	molecular weight of kth gaseous species, average molecular weight
X_k, Y_k	mole fraction and mass fraction of kth gaseous species
x, y, z	streamwise, transverse and lateral Cartesian coordinates, Fig. 1

Greek symbols

Γ	surface site density, Eq. (5)
λ_g	thermal conductivity of gas, Eq. (3)
μ	dynamic viscosity, Eq. (2)
ρ, ρ_o	density, Eqs. (1) and (2), fresh mixture density, Fig. 12
σ_m	surface species site occupancy, Eq. (5)
φ	hydrogen-to-oxygen equivalence ratio
$\dot{\omega}_k$	homogeneous molar production rate of kth species, Eq. (4)

Subscripts

IN	inlet
ig	homogeneous ignition
g	gas
k, m	indices for gas-phase and surface species
W	wall
x	streamwise component
y, r	transverse component in Cartesian and cylindrical coordinates

The catalytic chemistry of hydrogen oxidation over noble metals has been investigated in a number of studies and detailed mean-field reaction mechanisms have thereafter been constructed [19–23]. Development of heterogeneous kinetics for simple fuels, such as hydrogen, is nowadays greatly aided by advancements in *ab initio* simulations [24] and in spatially-resolved *operando* surface science measurements [25]. It terms of gas-phase chemistry, recent studies have improved the understanding of homogeneous kinetics for hydrogen and hydrogen-containing fuels at turbine relevant pressures [26–29]. For coupled heterogeneous and homogeneous combustion systems, however, there are only a few investigations (especially at elevated pressures) for hydrogen and hydrogen-containing fuels.

The homogeneous ignition of fuel-lean and fuel-rich H_2/air mixtures over Pt-coated stagnation flow surfaces has been investigated at atmospheric pressure in Bui et al. [30], establishing the impact of equivalence ratio on the ignition temperature. In situ laser-based measurements of major and minor species concentrations across the boundary layer of a Pt-coated channel-flow reactor at atmospheric pressure were reported in Appel et al. [31], providing validated hetero-/homogeneous reaction schemes for fuel-lean H_2/air mixtures and further addressing the catalytic and gas-phase chemistry interactions as well as the chemistry/transport coupling. Maestri et al. [21,32] investigated the hetero-/homogeneous combustion of fuel-rich H_2/air mixtures over Rh-based catalysts at atmospheric pressure in a nearly isothermal annular reactor with a channel gap of 2.1 mm; they reported that gas-phase chemistry was significant at temperatures above ca. 820 K. Mantzaras et al. [33] extended the work of Appel et al. [31] for pressures up to 10 bar; therein, experiments and simulations have shown that the intricate pressure and temperature dependence of hydrogen homogeneous ignition kinetics resulted in suppression of gaseous combustion for pressures above 4 bar, for non-preheated fuel-lean H_2/air mixtures, and for catalyst surface temperatures as high as 1200 K. More recently, Ghermay et al. [34] investigated experimentally and numerically the effect of fractional hydrogen preconversion on the subsequent homogeneous ignition characteristics of fuel-lean H_2/air mixtures over Pt at pressures up to 8 bar. Literature studies for hetero-/homogeneous combustion of hydrogen at turbine-relevant pressures (ca. 15 bar) and mixture preheats (up to 800 K) are still lacking. Moreover, it will be shown that for the upper range of examined pressures, $p \geqslant 12$ bar, the mechanisms controlling gas-phase combustion are markedly different than those at lower pressures. Finally, it is essential to ascertain the operating conditions (pressure, mixture preheat, catalytic wall temperature, reactor geometrical confinement and residence time) under which gas-phase chemistry plays a role, given the growing interest for catalytic combustion systems using either hydrogen or hydrogen-enriched fuels [5,23,35–38].

The present work undertakes an experimental and numerical investigation of the hetero-/homogenous combustion of fuel-lean (equivalence ratios up to 0.30) H_2/air mixtures over Pt, at pressures up to 15 bar and mixture preheats up to 790 K. Experiments were performed in an optically accessible, channel-flow catalytic reactor with a height of 7 mm. One-dimensional spontaneous Raman measurements provided the boundary layer profiles of major species over the catalyst surface and planar laser induced fluorescence (LIF) of the OH radical monitored homogeneous combustion. Computations were carried out with an elliptic 2-D code that included elementary catalytic and gaseous chemical reaction schemes and detailed transport. The main objectives were to assess the impact of pressure and mixture preheat on the homogeneous combustion characteristics of hydrogen over Pt surfaces and to provide validated hetero-/homogeneous chemical reaction schemes at turbine-pertinent conditions. Specific objectives were to identify the underlying physicochemical processes (gas-phase ignition chemistry, flame propagation characteristics, interaction of transport and chemistry) that control the importance of gaseous chemistry in practical catalytic reactor geometries. The regimes of significance for gas-phase chemistry in hydrogen-fueled hetero-/homogeneous

combustion systems have finally been delineated as a function of geometrical confinement and operating conditions relevant to either large-scale power generation systems or to microreactors.

This article is organized as follows. The experimental and numerical methodologies are presented in Sections 2 and 3, respectively. In Section 4.1, comparisons between measurements and predictions are used to assess the aptness of the employed reaction schemes and to illustrate the impact of high pressure and preheat on homogeneous combustion. The effects of gas-phase ignition chemistry and flame propagation characteristics on the ensuing homogeneous combustion are discussed in Section 4.2. Finally, delineation of the operating conditions under which gas-phase combustion cannot be ignored is undertaken in Section 4.3 for various practical geometrical confinements.

2. Experimental

2.1. High pressure test rig

The test rig has been used in earlier studies of hydrogen and hydrocarbon hetero-/homogeneous combustion [33,34,39,40] such that a brief description is provided next, with emphasis on modifications adopted for the present studies. Measurements were performed in an optically accessible, rectangular-shaped catalytic reactor, which was positioned inside a high-pressure cylindrical tank (Fig. 1). The reactor was made of two horizontal non-porous Si[SiC] ceramic plates (L = 300 mm long, 110 mm wide, 9 mm thick, positioned $2b$ = 7 mm apart) and two vertical quartz glass windows (3 mm thick, 12 mm high and 300 mm long) at a lateral separation of W = 104 mm (Fig. 1c). The resulting reactor volume was $300 \times 104 \times 7$ mm^3. The inner Si[SiC] plate surfaces were coated using plasma vapor deposition (PVD) first with a 1.5-μm thick nonporous Al_2O_3 layer and then with a 2.2-μm thick Pt layer. Such a thick Pt layer resembled a polycrystalline platinum surface and this was verified with detailed surface science measurements (BET, chemisorption and XPS, as discussed in [34,41]).

The axial temperature profile of each catalytic plate was measured with 12 S-type thermocouples, positioned along the x–y symmetry plane of the reactor (Fig. 1a) and embedded 0.9 mm beneath the catalytically coated surfaces. The axial locations of the thermocouples will be shown in the forthcoming Section 4. In channel-flow catalytic combustion of fuel/air mixtures with deficient reactants having Lewis numbers less than unity (as, for example, in fuel-lean H_2/air combustion where $Le_{H2} \sim 0.3$), superadiabatic surface temperatures are attained at the far upstream positions [31,33,34,42], which in turn endanger the catalyst and reactor integrity. To suppress such high surface temperatures, the approach of earlier hydrogen catalytic combustion studies was adopted [31,33,34], whereby the front facets of both Si[SiC] plates (110 mm × 9 mm) where firmly contacted to a water-cooled section of the reactor support frame (see Fig. 1a). At the same time, two resistive coils heated the ceramic plates over the length $100 < x < 300$ mm in order to counteract the increased heat losses at the reactor rear.

To better control the amounts of H_2 and O_2, which in turn affected the onset of homogeneous ignition, the oxidizer was not air but a mixture of separately supplied oxygen and nitrogen. High

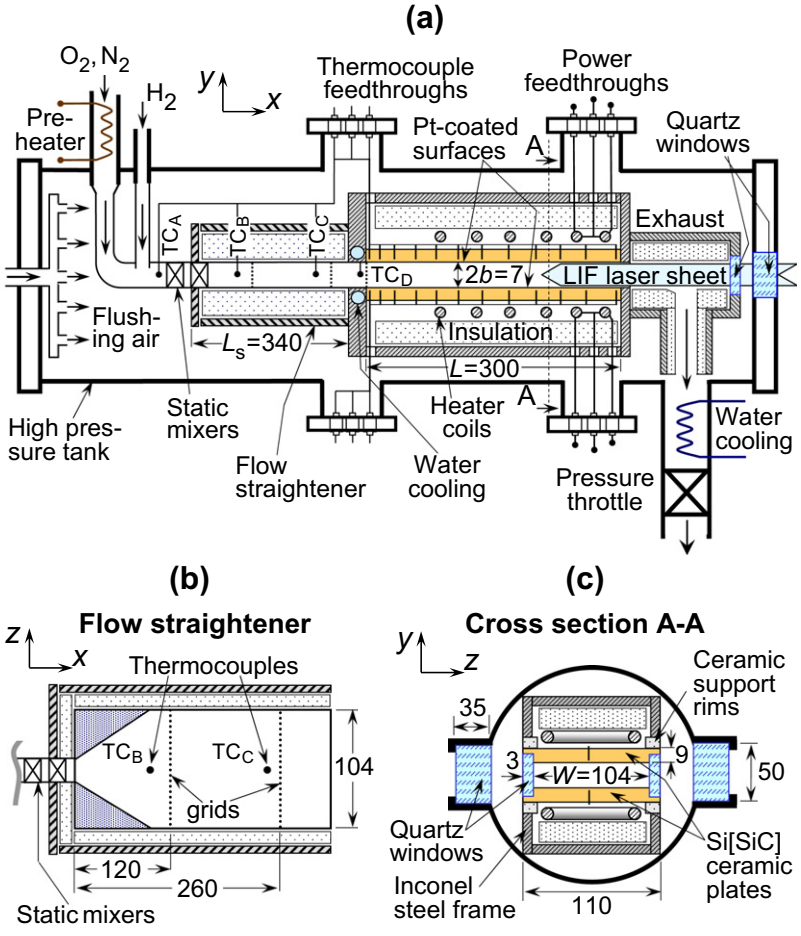

Fig. 1. (a) Schematic of the high-pressure test rig, (b) top view of the flow straightening unit, and (c) cross section of the catalytic channel reactor. All distances are in mm.

pressure bottles provided H_2, O_2 and N_2. The flows of these gases were regulated and measured by three dedicated Brooks mass-flow controllers with accuracies better than ±0.2%. The O_2 and N_2 flows were mixed and preheated with an electric heater, and then hydrogen was injected to the O_2/N_2 mixture 400 mm upstream of the reactor. Complete mixing of the fuel and oxidizer streams was achieved in two sequential static mixers. Experiments with preheated $H_2/O_2/N_2$ at high pressures were particularly demanding due to the resulting high mixture reactivity. A specifically designed flow-straightening section (Fig. 1b) equipped with cross-flow grids mitigated autoignition of the preheated reactive mixture and at the same time provided a uniform flow at the reactor entry. Autoignition mitigation was verified with a series of four sheathed K-type thermocouples (TC_A to TC_D, Fig. 1a), which monitored the mixture temperature from the point of hydrogen injection down to the reactor entry, while flow uniformity was assessed by hot-wire velocimetry measurements at the exit of the stand-alone flow straightening unit. Thermocouple TC_D, positioned 2 mm upstream of the reactor entry, also provided the inlet temperature needed for the numerical simulations. The high pressure tank was equipped with two 350-mm long, 50-mm high and 35-mm thick quartz glass windows, allowing optical access from both reactor sides (Figs. 1c and 2). Two additional quartz windows at the reactor exhaust and at the rear flange of the tank (Fig. 1a) provided a streamwise optical access. Finally, a continuous flow of air flushed any undesired combustion products from the free volume between the tank and the reactor assembly.

2.2. Laser diagnostics

The Raman and LIF techniques have been used in previous catalytic combustion works [31,34,40] and are thus concisely described below. In the LIF experiments (see Fig. 2), the 532 nm second harmonic beam of a pulsed Nd:YAG laser (Quantel TDL90 NBP2UVT3) pumped a tunable dye laser (Quantel TDL90). The dye output beam was frequency-doubled to 285 nm with a pulse energy of 0.5 mJ, low enough to avoid saturation of the $A(v=1) \leftarrow X(v'=0)$ OH transition. A cylindrical lens telescope and a 1-mm slit mask transformed this beam into a thin light sheet, which propagated counterflow along the x–y symmetry plane of the reactor (Figs. 1a and 2). Fluorescence from both (1–1) and (0–0) OH transitions at 308 and 314 nm, respectively, was collected at 90° through the reactor and side tank windows with an ICCD camera (LaVision Imager Compact HiRes IRO, 1392 × 1024 pixels). Channel areas of 100 mm × 7 mm were acquired on a 628 × 44 pixel area of the ICCD detector chip and the camera was traversed axially to record the entire 300 mm reactor length. To increase the signal-to-noise ratio, 400 images were averaged at each measuring position. The LIF signal was calibrated with absorption measurements performed with the 285 nm beam crossing the reactor laterally (z-direction) through all 4 reactor and tank side windows, as in [31,39].

For the Raman measurements, a frequency-doubled Nd:YLF high repetition rate pulsed laser (Quantronix Darwin Duo) was used, with output radiation at 526.5 nm. The laser was operated at 1.5 kHz with a pulse duration and energy of 130 ns and 43 mJ, respectively. The Raman beam was focused through the tank and reactor side-windows into a vertical line (~0.3 mm thick) by an f = 150 mm cylindrical lens (Fig. 2). The focal line spanned the 7 mm channel separation and was offset laterally (z = 15 mm) to increase the collection angle and minimize thermal beam steering [31,34]. Two f = 300 mm lenses collected the scattered light and focused it on a 25 cm imaging spectrograph (Chromex-250i) equipped with an ICCD camera (Princeton Instruments PI-MAX1024GIII). Up to 20,000 pulses were integrated on the detector chip when acquiring an image. Raman data were recorded at different axial positions by traversing a table supporting the sending and collecting optics as well as the Nd:YLF laser and the spectrograph (Fig. 2). The measurement accuracy was ~8% for species concentrations as low as 0.5 vol.% For concentrations lower than 0.5 vol.%,

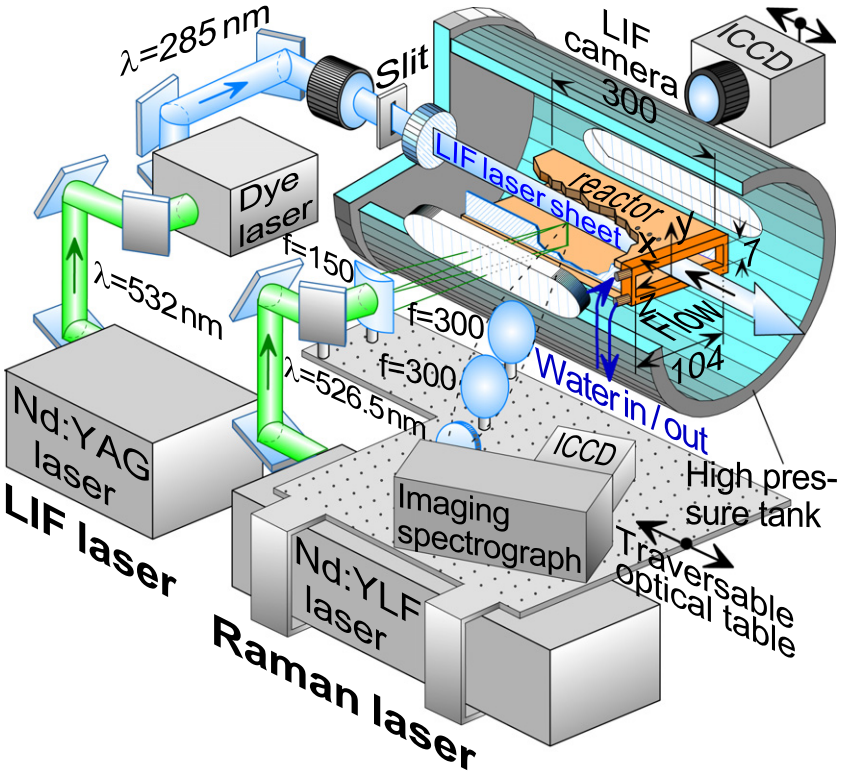

Fig. 2. OH-LIF and Raman optical setup arrangement in the high-pressure test rig. All focal lengths are in mm.

larger uncertainties were present. Raman data closer than 0.7 mm to both walls were discarded due to low signal-to-noise ratios. It is finally clarified that the Raman data could not assess the catalytic reactivity, since the high reactivity of hydrogen on Pt always yielded transport-limited conversion for the present wall temperatures.

3. Numerical

The governing equations (in their full elliptic form) were solved for a steady laminar reactive flow in 2-D Cartesian coordinates, simulating the 300 mm × 7 mm (x–y) channel domain (Fig. 1a). To further investigate the effect of confinement type (planar versus tubular channels, Section 4.3) on homogeneous combustion, additional simulations were carried out in cylindrical coordinates. The general form of the equations was the following:

Continuity equation:

$$\nabla \cdot (\rho \vec{u}) = 0. \tag{1}$$

Momentum equations:

$$\nabla \cdot (\rho \vec{u}\vec{u}) + \nabla p - \nabla \cdot \mu \left[\nabla \vec{u} + (\nabla \vec{u})^T - \frac{2}{3}(\nabla \cdot \vec{u})\underline{\underline{I}} \right] = 0. \tag{2}$$

Total enthalpy equation:

$$\nabla \cdot (\rho \vec{u} h) + \nabla \cdot \left(\sum_{k=1}^{Kg} \rho Y_k h_k \vec{V}_k - \lambda_g \nabla T \right) = 0. \tag{3}$$

Gas-phase species equations:

$$\nabla \cdot \rho Y_k (\vec{u} + \vec{V}_k) - \dot{\omega}_k W_k = 0, \quad k = 1, \ldots, K_g. \tag{4}$$

Surface species coverage equations:

$$\sigma_m \frac{\dot{s}_m}{\Gamma} = 0, \quad m = 1, \ldots, M_s. \tag{5}$$

For the present high Reynolds numbers (see Section 4.1) and the 7-mm narrow vertical channel gap, buoyancy was insignificant. The diffusion velocities $\vec{V}_k$ in Eqs. (3) and (4) were computed using mixture average diffusion, including thermal diffusion for the light species H and H_2 [43]:

$$\vec{V}_k = -D_{km} \nabla [\ln(Y_k \overline{W}/W_k)] + \left[D_k^T W_k / (\rho Y_k \overline{W}) \right] \nabla (\ln T). \tag{6}$$

The ideal gas and caloric state laws were finally used:

$$p = \frac{\rho R^o T}{W}, \quad h_k = h_k^o(T_o) + \int_{T_o}^{T} c_{p,k} dT \; k = 1, \ldots, K_g. \tag{7}$$

The interfacial boundary conditions for the gas-phase species and energy at the lower and upper catalytic walls ($y = 0$ and $y = 2b$, respectively) were:

$$(\rho Y_k V_{k,y})_{y=0} = W_k (\dot{s}_k)_{y=0}, \quad -(\rho Y_k V_{k,y})_{y=2b} = W_k (\dot{s}_k)_{y=2b} \tag{8}$$

and

$$T(x, y = 0) = T_{W,L}(x), \quad T(x, y = 2b) = T_{W,U}(x), \tag{9}$$

with $T_{W,U}(x)$ and $T_{W,L}(x)$ the temperature profiles of the upper and lower wall, respectively, fitted through the 12 thermocouple measurements of each plate. No-slip was applied for both velocity components at the gas–wall interfaces. At the inlet, uniform profiles were used for the temperature T_{IN} (measured at TC_D, Fig. 1a), the axial velocity U_{IN} and the species mass fractions. At the outflow, $v = 0$ was used for the transverse velocity and zero-Neumann conditions for all other scalars. A staggered grid of 420 × 100 points (x and y, respectively) was employed, with finer x-spacing closer to the entrance and y-spacing closer to both catalytic walls. The solution algorithm has been described elsewhere [31].

The detailed mean-field heterogeneous reaction scheme for the oxidation of H_2 over Pt from Deutschmann et al. [23] (11 irreversible and three reversible reactions, five surface and six gaseous species) was employed, with a platinum surface site density $\Gamma = 2.7 \times 10^{-9}$ mol/cm^2. Surface thermodynamic data for the reversible reactions were taken from [44]. For homogeneous chemistry, the mechanism of Li et al. [26] was used (21 reversible reactions and nine species) with its accompanying gas-phase thermodynamic data. This mechanism has been tested against shock tube, flow-reactor, and laminar flame speed measurements at pressures up to 87 bar. Gas-phase and surface reaction rates were evaluated with CHEMKIN [45] and Surface-CHEMKIN [46], respectively, while all transport properties were calculated from the CHEMKIN transport database [43].

4. Results and discussion

4.1. Homogeneous ignition measurements and predictions

Table 1 summarizes all experimental conditions. Measurements have been performed at pressures 1, 2, 6, 8, 10, 12 and 15 bar with mixture preheats (T_{IN}) ranging from 390 K to 790 K. With increasing mixture preheat, the hydrogen-to-oxygen equivalence ratios were reduced in order to avoid autoignition in the mixing or flow straightening sections upstream of the reactor (Fig. 1a and b). To this direction, equivalence ratios in the range $0.08 \leqslant \varphi \leqslant 0.30$ were used. Moreover, for a given pressure, the mass throughput ($\dot{M}$ in Table 1) was not kept constant but it generally increased with rising preheat to eliminate the risk of flame flashback. The inlet Reynolds numbers (Re_{IN} in Table 1), calculated from the uniform inlet properties and the channel hydraulic diameter (=13.1 mm), ranged from 1948 to 3330. It is clarified, however, that all cases could be treated with a laminar flow model: earlier turbulent catalytic combustion studies [47] have shown that the strong flow laminarization induced by the hot catalytic walls guaranteed laminar conditions at Re_{IN} higher than 8000 for channel wall temperatures above 1000 K.

Measured and predicted 2-D distributions of the OH radical over the entire channel length are provided in Fig. 3 ($1 \leqslant p \leqslant 6$ bar) and Fig. 4 ($8 \leqslant p \leqslant 15$ bar) for 21 of the total 26 cases in Table 1. As stated in Section 2.2, the measured OH maps in Figs. 3 and 4 have been constructed by connecting 100-mm-long, partially overlapping LIF images. Small temperature differences between the upper and lower catalytic walls led to a slight asymmetry in the flame shapes (see Figs. 3 and 4). Maximum temperature differences between the upper and lower walls ranged from 15 K (Case 7) to 40 K (Case 26), as indicated from the thermocouple measurements in Figs. 5 and 6. The axial location of homogeneous ignition (x_{ig}) is denoted with vertical arrows in Figs. 3 and 4; x_{ig} has been defined in both measurements and predictions as the far-upstream location whereby OH reached 5% of its maximum value inside the channel. Homogeneous ignition at pressures $p \geqslant 12$ bar could not be accurately determined with the LIF data. Most of the cases at 12 and 15 bar referred to OH concentrations less than 2 ppmv (see Fig. 4) and such low levels were not amenable to a planar measurement fluorescence technique. Nonetheless, qualitative agreement has been established between measurements and predictions in terms of the very narrow extent of the gaseous combustion zone away from both walls (see, for example, in Fig. 4 the flames of Cases 20, 22 and 24–26). Moreover, quantitative agreement for these high pressure cases was not of great concern since gas-phase combustion was altogether very weak as will be discussed later on in the context of Fig. 6.

The onset of homogeneous ignition was well predicted by the model, with the difference between measured and predicted

Table 1
Experimental conditions.[a]

Case	p (bar)	T_{IN} (K)	φ	H_2 (%)	O_2 (%)	U_{IN} (m/s)	Re_{IN}	$\dot{M}$ (g/s)	$x_{ig,m}$ (mm)	$x_{ig,p}$ (mm)
1	1	404	0.30	11.0	18.5	4.39	1948	2.50	16	13
2	1	578	0.17	6.6	19.5	9.04	2281	3.75	36	39
3	1	673	0.11	4.1	18.2	12.20	2441	4.45	54	62
4	1	760	0.08	2.8	18.0	13.24	2191	4.33	94	83
5	2	401	0.25	9.4	18.8	2.20	2008	2.56	46	35
6	2	576	0.17	6.5	19.5	4.70	2388	3.92	51	47
7	2	653	0.11	4.5	20.0	6.50	2726	4.88	82	73
8	6	398	0.25	7.9	15.9	0.84	2365	2.99	73	68
9	6	580	0.17	6.7	19.5	1.57	2361	3.89	65	74
10	6	676	0.11	4.1	17.8	2.53	3017	5.51	90	94
11	6	790	0.09	4.1	21.6	2.96	2724	5.55	84	96
12	8	406	0.25	9.3	18.8	0.68	2434	3.13	52	65
13	8	567	0.17	6.7	19.5	1.15	2395	3.89	62	72
14	8	676	0.11	4.1	19.2	2.05	3257	5.96	84	91
15	10	405	0.18	6.9	19.5	0.63	2897	3.73	89	77
16	10	575	0.17	6.5	19.6	1.12	2854	4.68	55	60
17	10	677	0.11	4.3	18.8	1.67	3302	6.05	88	78
18	10	763	0.10	4.5	21.8	1.72	2778	5.54	80	82
19	12	390	0.18	7.0	19.4	0.42	2456	3.02	–	–
20	12	576	0.17	6.4	19.6	0.98	2990	4.91	–	–
21	12	671	0.11	4.1	18.9	1.38	3330	5.60	106	93
22	12	780	0.10	4.4	21.6	1.48	2768	4.90	–	–
23	15	391	0.22	8.4	19.1	0.42	3032	3.80	–	–
24	15	585	0.15	6.0	19.7	0.79	2971	4.89	–	–
25	15	679	0.11	4.4	20.0	0.91	2684	4.93	–	–
26	15	758	0.10	4.3	21.3	1.17	2872	5.70	–	–

[a] Pressure, inlet temperature, equivalence ratio, species volumetric composition (the balance is N_2), inlet velocity and Reynolds number, mass flow rate, measured ($x_{ig,m}$) and predicted ($x_{ig,p}$) homogeneous ignition distances (x_{ig} are provided only for cases with predicted OH levels above 2 ppmv).

ignition distances being for most cases less than 10 mm (see Table 1). The same overall good agreement also applied for the ensuing flame shapes and lengths at $x \geqslant x_{ig}$. Finally, the maximum measured OH levels were within 20% of the corresponding computed values for all cases where a strong flame could be established and could thus facilitate calibration of the LIF signal with absorption measurements. Good agreement has thus been established between measurements and predictions in terms of homogeneous ignition location, flame shapes and absolute OH levels. This was an important initial result of this study, clearly showing the applicability of the employed hetero-/homogeneous reaction mechanisms at high pressures and preheats relevant to gas turbine applications.

Computed catalytic (C) and gaseous (G) axial profiles of hydrogen conversion rates are shown in Fig. 5 for the three cases at $p = 2$ bar and in Fig. 6 for 12 selected cases at the higher pressure range $8 \leqslant p \leqslant 15$ bar; the same figures also provide axial profiles of the y-averaged hydrogen mass fraction. The predicted C rates accounted for catalytic conversion on both channel surfaces, whereas the G rates were computed by integrating the volumetric gaseous hydrogen conversion over the 7 mm channel height. The 12 cases in Fig. 6 were not all the same with those in Fig. 4; for example, predictions with low preheats are shown in Fig. 6 (Cases 19 and 23) but such conditions had too low an OH LIF signal for inclusion in Fig. 4. The predicted homogeneous ignition distances, denoted by the vertical arrows in Figs. 5 and 6, attested that the OH-based definition of homogeneous ignition closely corresponded to the rise in the homogeneous hydrogen conversion rate G. To facilitate comparisons of catalytic (C) and most importantly of gas-phase (G) conversion rates between cases with different operating parameters (mass flow rates, equivalence ratios), the maxima in the ordinates of the three plots in Fig. 5 have been scaled with the corresponding inlet hydrogen mass fluxes, $Y_{H2,IN}\,\dot{M}/(2b \times W)$, of each case. The same procedure has also been adopted for all 12 cases shown in Fig. 6.

For the lowest preheats $T_{IN} = 398$–406 K, strong flames were established in the reactor for pressures $1 \leqslant p \leqslant 8$ bar, as seen by the OH LIF measurements and the numerical predictions in Fig. 3 (Cases 1, 5 and 8) and Fig. 4 (Case 12), as well as by the G conversion rates in Fig. 5 (Case 5) and in Fig. 6a (Case 12). As the pressure increased to 12 bar, the G rate at the lowest preheat (Fig. 6c, Case 19 with $T_{IN} = 390$ K) became negligible and the same was also evident at 15 bar (Fig. 6d, Case 23 with $T_{IN} = 391$ K). Earlier studies [33] with practically non-preheated ($T_{IN} = 310$ K) H_2/air mixtures at pressures of up to 10 bar, have shown that gas-phase combustion was largely suppressed for $p \geqslant 4$ bar. The present results indicate that for modest preheats of ~390 K the suppression of gaseous combustion is shifted to appreciably higher pressures, $p \geqslant 12$ bar. For $p = 12$ bar gas-phase conversion was appreciable only for $T_{IN} \geqslant 576$ K (see Fig. 6c, Cases 20 and 22), whereas for $p = 15$ bar gas-phase combustion was insignificant even at preheats as high as 758 K (Fig. 6d, Case 26).

The axial profiles of computed average hydrogen mass fraction shown in Fig. 6 indicated that for the higher pressure cases there was always a hydrogen breakthrough at the reactor exit. This effect was more pronounced at $p = 15$ bar due to the lack of appreciable gaseous hydrogen consumption. For $p \geqslant 10$ bar, a non-vanishing catalytic C conversion was evident even at $x > x_{ig}$, leading to combined hetero-/homogeneous combustion well inside the axial extent of the gaseous combustion zone. Moreover, as the G conversion dropped at the reactor rear, the C conversion started rising (see, for example, Case 18 in Fig. 6b and Cases 20 and 22 in Fig. 6c). In contrast, for the lower pressure $p = 2$ bar in Fig. 5, whereby gaseous combustion was stronger, the catalytic conversion C practically ceased shortly after the onset of homogeneous ignition.

In summary, a modest increase in mixture preheat from 310 to ~390 K sufficed to restore homogeneous combustion for pressures up to 10 bar, which was a pressure range of interest for small-scale industrial turbines and also for microturbine-driven portable

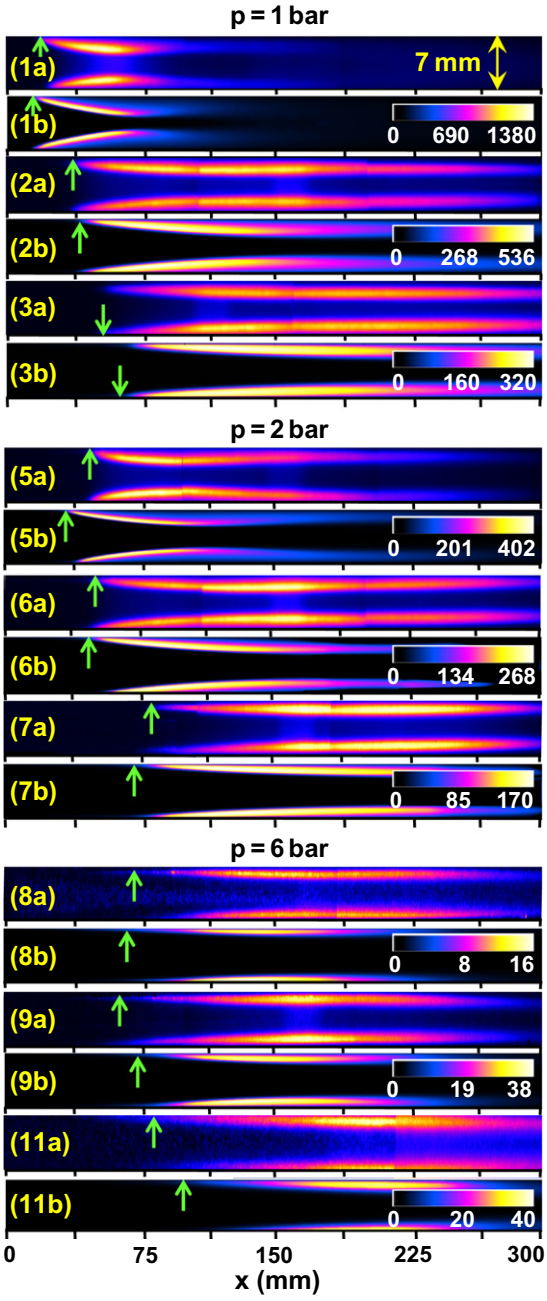

Fig. 3. (a) LIF-measured and (b) numerically-predicted OH 2-D maps for nine selected cases in Table 1 at pressures of 1, 2 and 6 bar. The vertical arrows define the onset of homogeneous ignition. For each case, the color bars provide the minimum and maximum computed OH in ppmv. (For interpretation of the references to color in this figure legend, the reader is referred to the web version of this article.)

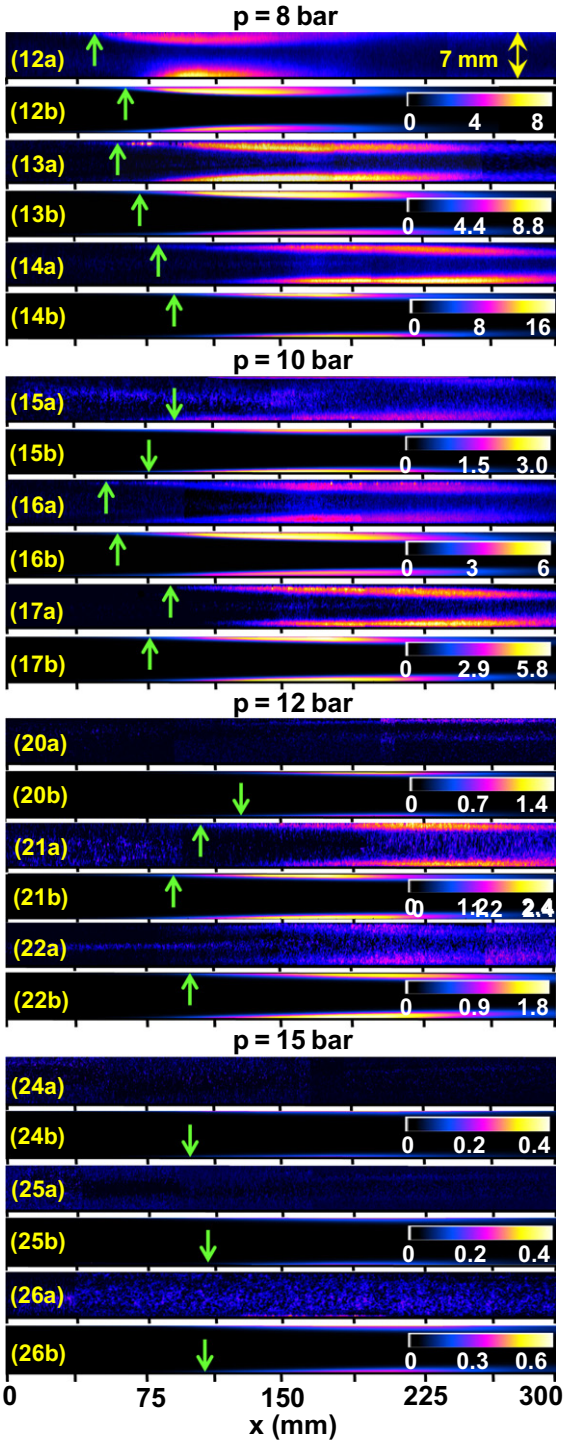

Fig. 4. (a) LIF-measured and (b) numerically-predicted OH 2-D maps for 12 selected cases in Table 1 at pressures of 8, 10, 12 and 15 bar. The vertical arrows define the onset of homogeneous ignition. For each case, the color bars provide the minimum and maximum computed OH in ppmv. (For interpretation of the references to color in this figure legend, the reader is referred to the web version of this article.)

power generation systems [48]. On the other hand, as pressure increased above 10 bar the preheat requirements for significant gas-phase conversion raised appreciably. For $p = 15$ bar, which was a pressure relevant for large gas turbines, even preheats up to 758 K, typical to full load operation, were not adequate to initiate significant gas-phase conversion at the examined geometrical confinement of 7 mm. Restoration of appreciable gaseous combustion at $p = 5$ and 8 bar has also been reported in [34] by preconverting part of the fuel. Fuel preconversion raised the effective inlet temperature and in this respect the previous findings were in agreement with the present study. However, apart from the limited pressure range studied in [34] ($1 \leqslant p \leqslant 8$ bar), fuel preconversion resulted in inlet temperatures of at least 580 K, thus precluding detailed studies at intermediate preheats. An additional complication in [34] was that the preconversion led to formation of water and radicals; the former was a strong inhibitor of gaseous combustion while the latter affected appreciably the ignition characteristics at atmospheric pressure. The results of the present study have

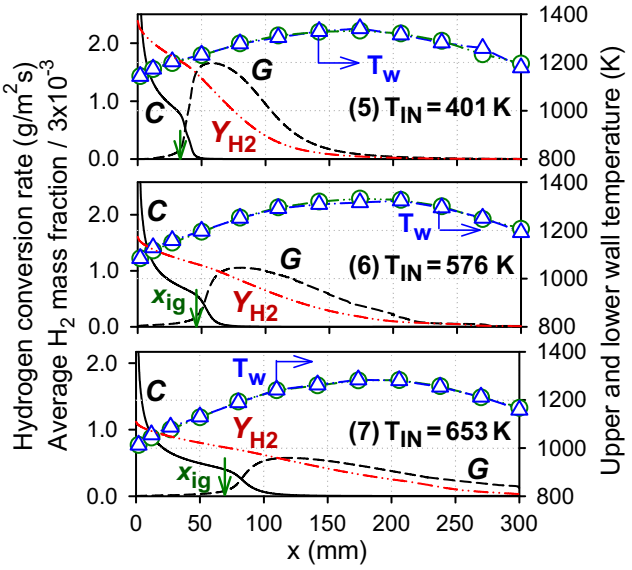

Fig. 5. Thermocouple measurements (upper wall: triangles; lower wall: circles) and fitted axial temperature profiles through the measurements (lines). Computed catalytic (C) and gas-phase (G) hydrogen conversion rates (solid and dashed lines, respectively) and the average (over the 7 mm channel height) axial profiles of hydrogen mass fraction, Y_{H2} (dashed double-dotted lines). The vertical arrows define the computed location of homogeneous ignition (x_{ig}). Cases 5, 6 and 7 in Table 1 at $p = 2$ bar.

demarcated the regimes of mixture preheat and pressure for which gas-phase combustion was important. The reasons for the gas-phase combustion behavior discussed in Figs. 3–6 will be elaborated in Section 4.2.

The preceding statements regarding the effect of pressure and preheat on gas-phase chemistry presumed that the catalytic processes were also well-reproduced by the numerical model. An incorrect prediction of the catalytic fuel conversion over the gas-phase induction length could greatly affect the location of homogeneous ignition and thus falsify the gaseous kinetics. To further increase complication, analytical studies have shown the existence of multiple combinations of catalytic and gaseous reactivities yielding the same homogeneous ignition distance [49]. Although the measured post-ignition flame shapes could be used to eliminate most of these combinations, the Raman measurements provided the only secure way of ensuring that the catalytic processes preceding homogeneous ignition were well-predicted. Comparisons between Raman-measured and numerically-predicted transverse profiles of H_2 and H_2O mole fractions are shown in Fig. 7 for two cases in Table 1 (pressures of 2 and 12 bar) and two axial positions preceding homogeneous ignition ($x < x_{ig}$). The numerical predictions indicated a catalytic conversion close to the transport-limit, as evidenced by the practically vanishing hydrogen levels near both walls ($y = 0$ and 7 mm). This behavior was also reproduced by the measurements, despite the lack of Raman data at distances closer than 0.7 mm to both catalytic walls.

4.2. Gas-phase combustion

The experimental conditions in Table 1 and the resulting flames in Figs. 3 and 4 pertained to different mass throughputs, equivalence ratios (and, sometimes, for a given equivalence ratio different absolute H_2 and O_2 volumetric contents) and also varying wall temperatures. Such differences were necessary to anchor stable flames inside the channel reactor at widely varying mixture preheats and pressures. However, to understand the impact of gas-phase chemistry and transport on the onset of homogeneous ignition over Pt surfaces, comparisons were required between cases where only a limited number of parameters changed while maintaining the others constant. To this direction, detailed simulations have been performed using two different numerical platforms and the validated hetero-/homogeneous chemistries of Section 4.1.

4.2.1. Homogeneous chemistry kinetics

In a first step, pure gas-phase ignition characteristics of hydrogen (without the inclusion of catalytic reactions) were investigated. Ignition delays of H_2/air mixtures at equivalence ratios $\varphi = 0.30$ and 0.10 and pressures from 1 to 15 bar, relevant to the conditions in Table 1, have been computed in a constant pressure non-catalytic batch reactor using the SENKIN package of CHEMKIN [50]. Ignition delays were defined as the times where the hydrogen mass fraction dropped to 50% of its initial value. Initial temperatures ranging from 950 to 1300 K were studied. These temperatures were higher than the mixture preheats in the channel reactor (see Table 1), so as to mimic the presence of the hot catalytic walls that further preheated the flowing reacting gas. Figure 8 provides the inverse of the computed ignition delays (quantities proportional to the hydrogen gaseous reactivity) as a function of pressure with parameter the initial temperature. The trends discussed next were common for both investigated equivalence ratios. For the lowest examined initial temperature of 950 K, the gaseous reactivity decreased rapidly with rising pressure up to ~2 bar and then changed modestly for $p \geqslant 2$ bar. For the higher temperatures 1000 K $\leqslant T \leqslant$ 1300 K, the gaseous reactivity initially increased monotonically with rising pressure, peaked at a critical pressure p_{cr}, and subsequently dropped for $p > p_{cr}$. With rising initial temperature, p_{cr} increased and at the same time the drop in reactivity for $p > p_{cr}$ was reduced. Characteristically, at $T = 1250$ K the reactivity increased monotonically from 1 bar to $p_{cr} = 11.2$ bar and then dropped modestly for $p > p_{cr}$ such that the reactivity at $p = 15$ bar was only 12% lower than that at p_{cr}. This rich behavior in hydrogen ignition chemistry was a result of the competition between the chain branching step $H + O_2 \Longleftrightarrow O + OH$, the chain terminating step $H + O_2 + M \Longleftrightarrow HO_2 + M$, and also of the chain branching sequence $HO_2 + H_2 \Longleftrightarrow H_2O_2 + H$ and $H_2O_2 + M \Longleftrightarrow 2\,OH + M$ that became important at higher temperatures [51].

Although no direct comparisons could be made between the channel reactor experiments in Figs. 3 and 4 with the present ideal batch reactor predictions, the restoration of gaseous combustion at elevated pressures with rising preheat could be qualitatively understood from Fig. 8. In the channel reactor, the effective temperatures shown in Fig. 8 were a weighted average between the inlet and wall temperatures, with an added weight on the latter. In previous hetero-/homogeneous combustion studies of H_2/air mixtures with essentially no preheat ($T_{IN} = 310$ K) [33], the resulting effective temperatures were moderate enough, such that the gaseous reactivity was highest at pressures close to 1 bar, dropping rapidly for pressures above 2–3 bar (see for example the 950 and 1000 K curves in Fig. 8). For a hetero-/homogeneous combustion system this implied that the catalytic pathway could favorably compete against the homogeneous pathway by consuming significant amounts of hydrogen during the elongated gas-phase induction zones for $p \geqslant 4$ bar, thus suppressing flame formation. It is emphasized that the suppression of homogeneous combustion for $p \geqslant 4$ bar and $T_{IN} \sim 310$ K reported in [33] was an outcome not only of intrinsic hydrogen gas-phase kinetics but also of competition between gaseous and catalytic reactions for hydrogen consumption. It is further noted that the catalytic pathway was very effective in consuming hydrogen due the large molecular diffusivity and the very high reactivity of this species on platinum, even at moderate surface temperatures. On the other hand, a modest increase in preheat from 310 K to ~390 K (see Table 1) increased

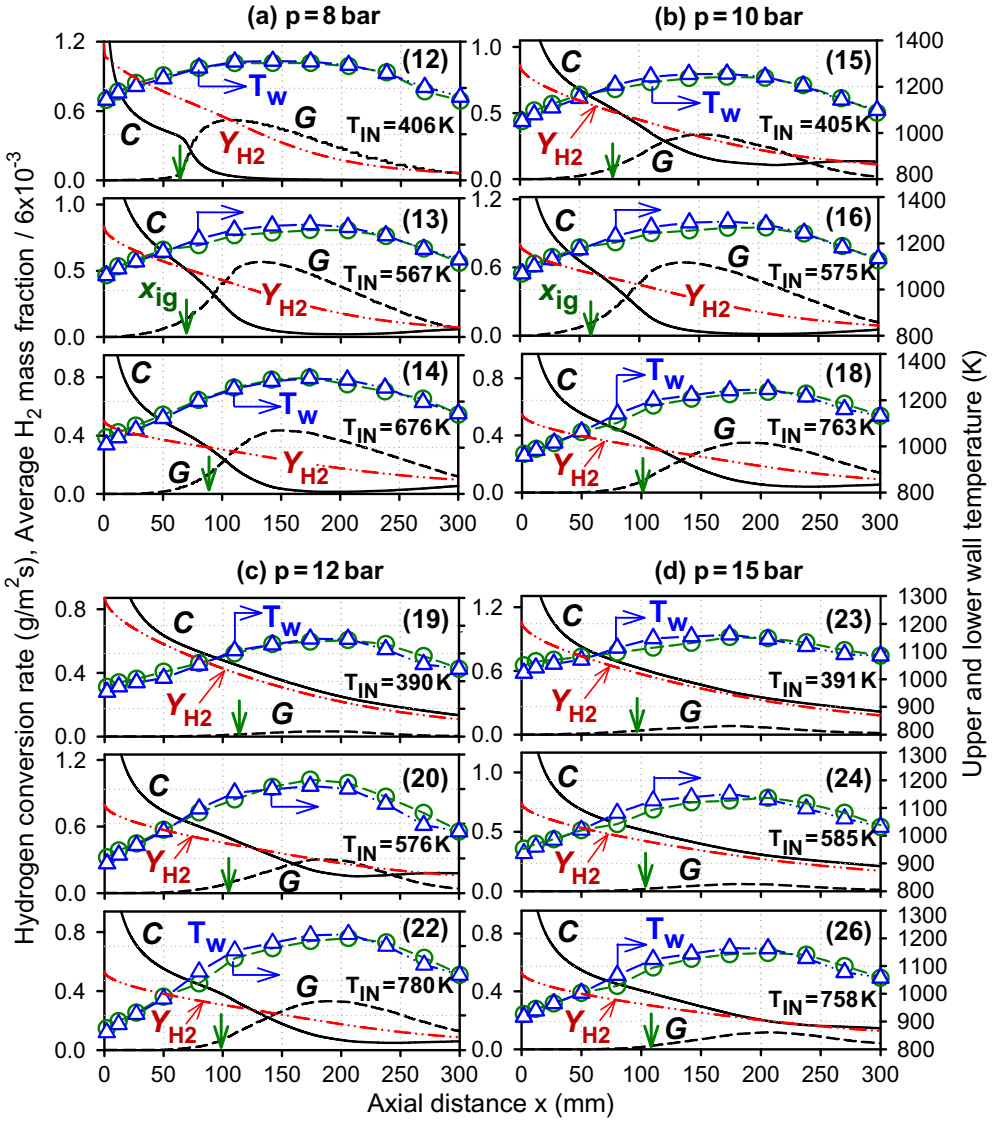

Fig. 6. Thermocouple measurements (upper wall: triangles; lower wall: circles) and fitted axial temperature profiles through the measurements (lines). Computed catalytic (C) and gas-phase (G) hydrogen conversion rates (solid and dashed lines, respectively) and the average (over the 7 mm channel height) axial profiles of hydrogen mass fraction, Y_{H2} (dashed double-dotted lines). The vertical arrows define the computed location of homogeneous ignition (x_{ig}); (a) Cases 12, 13 and 14 at p = 8 bar, (b) Cases 15, 16 and 18 at p = 10 bar, (c) Cases 19, 20 and 22 at p = 12 bar, and (d) Cases 23, 24 and 26 at p = 15 bar.

the value of p_{cr} and further reduced the disparity in reactivities between the lower ($p < p_{cr}$) and higher pressure regimes ($p > p_{cr}$). This extended the upper pressure limit for the existence of appreciable gaseous combustion to 10 bar (see Fig. 4).

The previous qualitative analysis, based mainly on gas-phase ignition chemistry arguments and consideration of the competition between the heterogeneous and homogeneous pathways, could account for the observed re-establishment of gaseous combustion at pressures up to 10 bar when increasing the preheat from 310 to ~390 K. However, it failed to explain the observed lack of strong gaseous combustion at $p > 10$ bar and high preheats. In this pressure range, the gaseous reactivity either increased modestly with rising pressure ($T < 1050$ K) or it dropped modestly with increasing pressure (e.g., $T = 1050$, 1100, 1250, and 1300 K in Fig. 8). It will be shown in the next section that at high pressures the presence of gaseous combustion was dictated not only by homogeneous ignition chemistry but also by flame propagation characteristics.

4.2.2. Flame propagation characteristics

Detailed simulations have been performed using as numerical platform tubular catalytic channels with diameter $d = 1.0$ mm and lengths sufficient to achieve at least 99.5% hydrogen conversion. The adopted geometry was more typical to that encountered in individual channels of practical honeycomb catalytic burners [52] compared to the larger, 7 mm gap, optically accessible reactor used in the experiments. Uniform wall temperatures, T_w, were imposed and the pressure was varied between 1 and 15 bar. Hydrogen/air mixtures with $\varphi = 0.30$ were investigated at two different total mass fluxes. The larger one, $\dot{m} = 42.4$ kg/m^2 s, referred to gas-turbine applications (resulting in a reference inlet velocity $U_{IN} = 18$ m/s at $p = 5$ bar and $T_{IN} = 673$ K) while the smaller one, $\dot{m} = 1.1$ kg/m^2 s, pertained to microreactors ($U_{IN} = 0.48$ m/s at $p = 5$ bar and $T_{IN} = 673$ K). This approach facilitated comparisons between cases having the same $\dot{m}$ and mixture preheat but different pressures, by maintaining a constant inlet Reynolds number. This was because analytical studies in channel-flow geometries

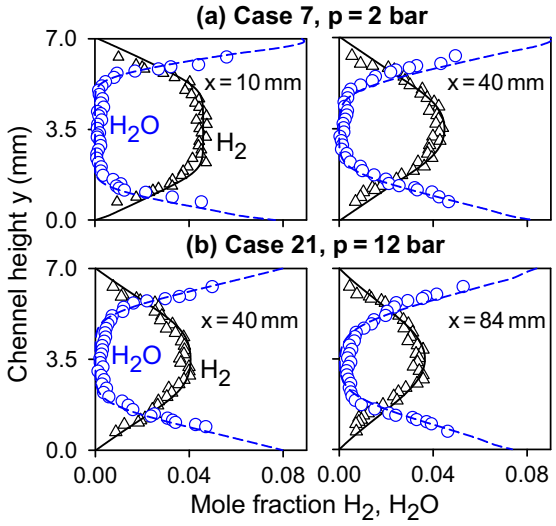

Fig. 7. Numerically predicted (lines) and Raman-measured (symbols) transverse profiles of H_2 and H_2O mole fractions at two selected axial positions: (a) Case 7 and (b) Case 21 in Table 1. H_2 (solid lines, triangles), H_2O (dashed-lines, circles). The axial positions are: x = 10 and 40 mm in (a) and x = 40 and 84 mm in (b).

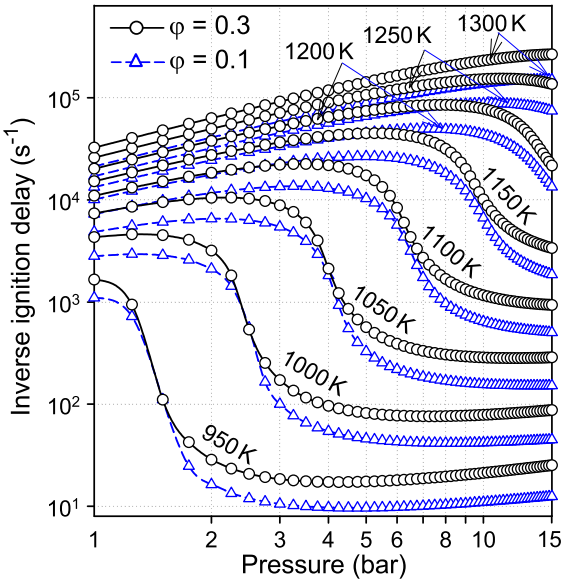

Fig. 8. Computed inverse ignition delays of fuel-lean H_2/air mixtures in a constant pressure non-catalytic batch reactor, at different pressures and temperatures. Equivalence ratios φ = 0.30 (circles) and φ = 0.10 (triangles).

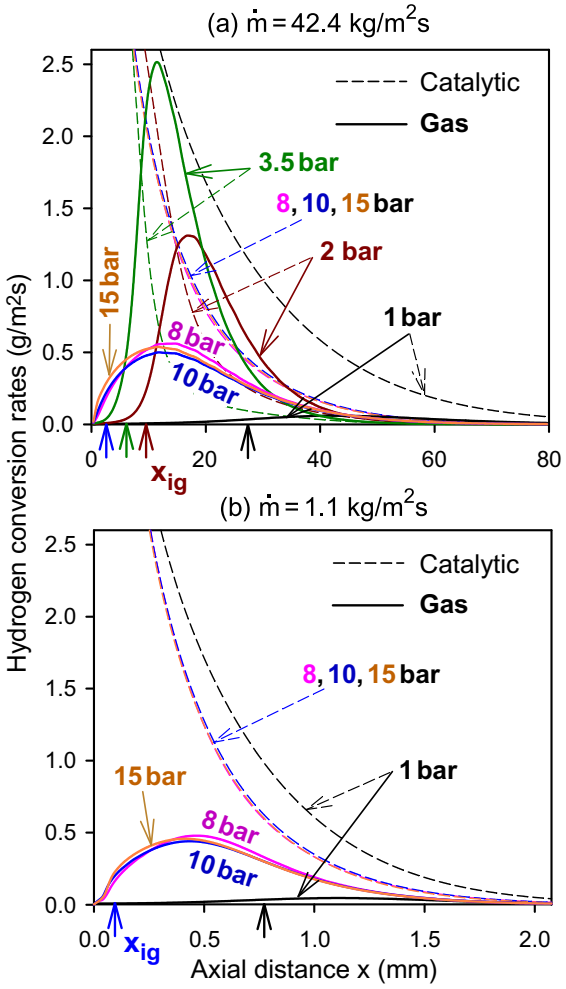

Fig. 9. Computed axial profiles of catalytic (C, dashed lines) and gas-phase (G, solid lines) hydrogen conversion rates for a φ = 0.30 H_2/air mixture in a tubular channel with diameter d = 1 mm, constant wall temperature T_w = 1350 K and inlet temperature T_{IN} = 673 K, at different pressures; (a) mass flux $\dot{m}$ = 42.4 kg/m^2 s, and (b) $\dot{m}$ = 1.1 kg/m^2 s. The channel lengths in (a) and (b) scale according to the $\dot{m}$ ratio. The vertical arrows in the x-axes define the locations of homogeneous ignition (x_{ig} = 27.4, 9.3, 6.1, 2.5, 2.5 and 2.3 mm for p = 1, 2, 3.5, 8, 10 and 15 bar, respectively in (a), and x_{ig} = 0.75, 0.10, 0.09 and 0.09 mm for p = 1, 8, 10 and 15 bar, respectively). For p = 2 and 3.5 bar in (b), the flames anchored directly at x = 0.

have shown [49,53] that, for the same Re_{IN}, the catalytic fuel conversion and the onset of homogeneous ignition only depended on the hetero-/homogeneous kinetics when other parameters, e.g. geometrical, transport, wall and inlet temperatures were the same. Finally, the flows were laminar with Re_{IN} up to 2000 for the higher max flux cases.

Predicted catalytic (C) and gaseous (G) hydrogen conversion rates are shown in Fig. 9 for various pressures, T_{IN} = 673 K, T_w = 1350 K, for both the high (Fig. 9a) and the low (Fig. 9b) mass flux conditions. The selected wall temperature of 1350 K constituted a likely upper limit that could be tolerated by reactor materials (metallic or ceramic) and catalysts during long-time operation. Reactor lengths of 80 mm were sufficient to convert at least 99.5% of the hydrogen at the highest mass flux $\dot{m}$ = 42.4 kg/m^2 s. The axial locations of homogeneous ignition, defined as in Section 4.1, are also shown with vertical arrows in Fig. 9. Concentrating first on the high mass flux conditions (Fig. 9a), a very weak gas-phase (G) combustion was evident at 1 bar; nonetheless, a homogeneous ignition position x_{ig} could still be numerically determined. With increasing pressure, the homogeneous ignition distance x_{ig} became progressively shorter and for the higher pressures of 8, 10 and 15 bar, the flames anchored close to the channel entry ($x_{ig} \approx 2$ mm). This behavior was consistent with the homogeneous ignition trends discussed in Fig. 8. For the high wall temperature T_w = 1350 K and for the large preheat T_{IN} = 673 K in Fig. 9a, a high temperature curve in Fig. 8 (e.g. 1250 or 1300 K) could explain the observed ignition behavior. Therein, the reactivity was lowest at 1 bar such that for the present 1 mm narrow channel (large surface-to-volume ratio) the catalytic pathway could effectively compete against the gaseous pathway for hydrogen consumption, resulting in a minute G rate. Characteristically, at the ignition location x_{ig} = 27.4 mm for p = 1 bar in Fig. 9a, the catalytic pathway had already consumed 88% of hydrogen. Therefore, the suppression of gaseous combustion at atmospheric pressure and high wall/preheat temperatures was a result of slow gaseous ignition chemistry in conjunction with the

increased hydrogen consumption from the catalytic pathway at large geometrical confinements (small channel diameters). The effect of confinement, in particular, should not be understated; it could account for strong gas-phase combustion at 1 bar for larger hydraulic diameter channels (as the 7-mm height channel used in the experiments, see Fig. 3).

As pressure increased in Fig. 9a, the gaseous reactivity also increased (at least for pressures up to 10 bar (see Fig. 8 for temperatures of 1250 or 1300 K), and thus x_{ig} was accordingly reduced. At $p > 10$ bar, the reactivity could either increase ($T = 1300$ K in Fig. 8) or drop modestly ($T = 1250$ K in Fig. 8) but x_{ig} was not affected as much, since ignition was already achieved close to the channel entry. It was surprising, however, that although the higher pressure cases $p \geqslant 8$ bar ignited farther upstream compared to the $p = 2$ and 3.5 bar cases in Fig. 9a, their integrated G conversion rates over the entire channel length were substantially lower. For example, the integrated G rate amounted to 38% of the total hydrogen conversion at 3.5 bar and to only 14% at 15 bar. It is further noted that the highest examined preheat $T_{IN} = 773$ K exhibited qualitatively the same behavior as the $T_{IN} = 673$ K cases in Fig. 9a.

Figure 10a–c provides computed isocontours of the hydrogen gas-phase reaction rates, 2-D distributions of the hydrogen mass fraction, and the hydrogen radial fluxes $\rho Y_{H2}(v + V_{H2,r})$ (denoted by vertical arrows at selected positions in the channel) for the high mass flux cases $\dot{m} = 42.4$ kg/m^2 s at 2, 3.5, and 15 bar. Five hydrogen gas-phase reaction isocontours are shown, with the outer one corresponding to 10% of the maximum hydrogen reaction rate of each case. Since Re_{IN} was the same in Fig. 10a–c, the hydrogen radial fluxes at the three different pressures would have been identical at the same locations provided that the catalytic hydrogen conversion was transport limited and that gaseous reactions were absent [53]. The nearly transport-limited catalytic conversion could readily be attested from the hydrogen mass fraction radial profiles in Fig. 11, pertaining to the 15 bar case in Fig. 10c (the same behavior was also attained for the other pressure cases). Gas-phase reactions modified the radial hydrogen fluxes, but for the cases shown in Fig. 10a–c the mass flux loading on the flames was still largely dictated by the inlet mass flow rate (or equivalently Re_{IN}) and the catalytic surface conversion, as explained next.

Following homogenous ignition, the hydrogen gaseous combustion zone was confined close to the catalytic walls. This has already been shown in the optically accessible reactor measurements and predictions (see Figs. 3 and 4) and was further evident from the reaction rate isocontours in Fig. 10a–c. The confinement of the gaseous reaction zone near the wall, which was largely an outcome of the low Lewis number of hydrogen (see also [31,34]), had profound implications for the ensuing flame stability. As the flames were aligned mostly parallel to the x-axis (for this, further consider that the y-axis scale in Fig. 10 has been stretched by a factor of 25 in comparison to the x-axis scale), flames with higher burning rates could position themselves farther away from the wall, at locations of higher radial hydrogen fluxes (dictated by the inlet flow rate and the catalytic reactivity). Laminar burning rates computed for freely propagating 1-D flames using the CHEMKIN package [54], have been plotted as a function of pressure in Fig. 12 for two H_2/air equivalence ratios, $\varphi = 0.30$ and 0.20, and two preheats, $T_o = 673$ K and 773 K. This was to mimic the increase in mixture preheat and drop in hydrogen content with increasing axial distance along the channel centerline (see temperature and H_2 mass fraction profiles in Fig. 11).

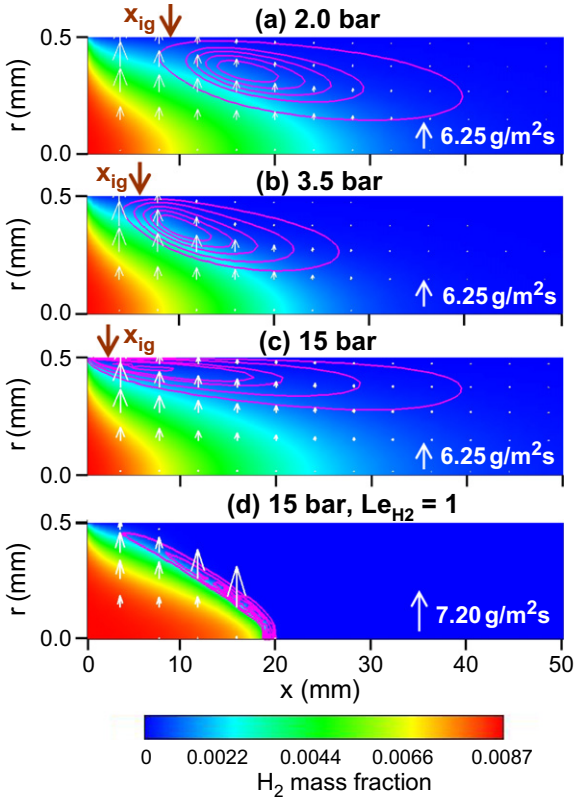

Fig. 10. (color online). Computed 2-D color maps of the hydrogen mass fraction, five isocontours of the hydrogen gas-phase reaction rates, and radial hydrogen fluxes $\rho Y_{H2}(v + V_{H2,r})$ denoted by vertical arrows for a $\varphi = 0.30$ H_2/air mixture in a $d = 1$ mm tubular channel at a mass flux $\dot{m} = 42.4$ kg/m^2 s, constant wall temperature $T_w = 1350$ K and inlet temperature $T_{IN} = 673$ K: (a) 2 bar, (b) 3.5 bar, (c) 15 bar, and (d) 15 bar but with the Lewis number of hydrogen artificially set to unity. The maximum gas-phase hydrogen reaction rates are 10, 20, 6 and 400 kg/m^3 s in (a) to (d), respectively. The color bar provides the hydrogen mass fraction levels and the arrows marked x_{ig} in (a), (b) and (c) the locations of homogeneous ignition. The channel centerline is located at $r = 0$ and the gas–wall interface at $r = 0.5$ mm.

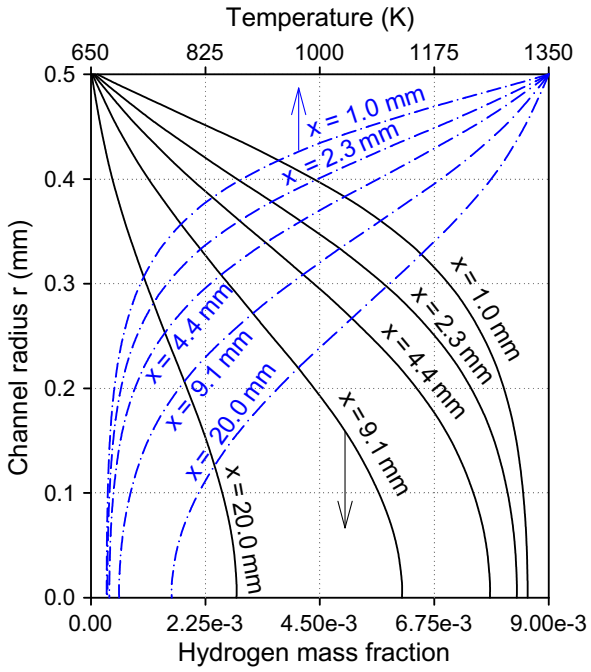

Fig. 11. Computed radial profiles of hydrogen mass fraction (solid lines) and temperature (dashed-dotted lines) in a tubular channel with diameter of 1 mm, at five selected axial positions. Hydrogen/air mixture with $\varphi = 0.30$, pressure 15 bar, wall temperature $T_w = 1350$ K, inlet temperature $T_{IN} = 673$ K and mass flux $\dot{m} = 42.4$ kg/m^2 s (inlet velocity $U_{IN} = 6$ m/s). The channel centerline is located at $r = 0$ and the gas–wall interface at $r = 0.5$ mm.

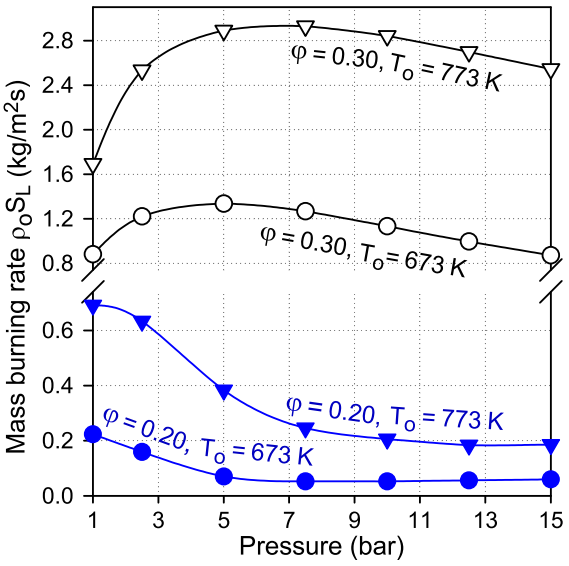

Fig. 12. Computed 1-D laminar burning rates as a function of pressure for $\varphi = 0.30$ and 0.20 H_2/air mixtures with upstream temperatures $T_o = 673$ and 773 K.

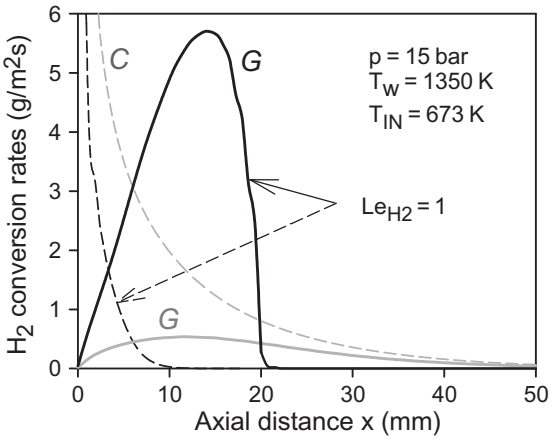

Fig. 13. Computed catalytic (C, dashed lines) and gas-phase (G, solid lines) hydrogen conversion rates for a tubular channel with diameter $d = 1$ mm, $T_w = 1350$ K, $T_{IN} = 673$ K, inlet equivalence ratio $\varphi = 0.30$ and $p = 15$ bar. Gray lines: normal transport properties for H_2; black lines: Lewis number of H_2 set to unity.

For $T_o = 673$ K and $\varphi = 0.30$, the burning rate at 15 bar was 34% lower than the corresponding peak value at ~5 bar, while for $T_o = 673$ K and $\varphi = 0.20$ the burning rate at 15 bar was 73% lower than the peak value at 1 bar; similar trends were apparent for the higher preheat of $T_o = 773$ K. The drop in laminar burning rates at the higher examined pressures led to a push of the gaseous reaction zone closer to the wall, wherein the radial hydrogen fluxes were lower, then to an increased leakage of hydrogen through the gaseous reaction zone and finally to catalytic conversion of the escaped fuel at the wall. This was evident in Figs. 9a and 10b and c when comparing the 3.5 and 15 bar cases. For distances $x > x_{ig}$, the catalytic C conversion was very weak at 3.5 bar and stronger at 15 bar (Fig. 9a), such that the radial hydrogen fluxes practically vanished near the wall for the former case (see Fig. 10b for $x > x_{ig}$). Analytical studies of gaseous combustion over stagnation flow catalytic surfaces have reported a similar behavior for limiting reactants with Lewis numbers less than unity [55]. Therein, a successive increase of the strain rate pushed the flame against the wall, leading to catalytic fuel conversion of the leaked fuel and finally to flame extinction. In the present channel-low geometry the aerodynamic strain – as represented by the imposed radial hydrogen fluxes – was the same at all pressures but the laminar burning rate dropped considerably at the highest examined pressures. It is emphasized that the gaseous burning rates were, for all cases, not strong enough to drastically alter the hydrogen radial fluxes in the zones between the outer edge of the flame (defined by the 10% reaction isocontour) and the channel centerline; this was manifested by the radial hydrogen mass flux arrows in Fig. 10a–c that had roughly the same magnitude. It is also clarified that the foregoing ignition analysis in Section 4.2.1 and the present propagation analysis were based on different characteristic temperatures. For the ignition analysis (Fig. 8), higher temperatures was relevant since homogeneous ignition was initiated close to the hot wall, as shown by high activation energy analytical studies [49,53]. On the other hand, lower temperatures were relevant for the propagation characteristics, since the fresh mixture supplied radially to the nearly horizontal flames originated from the channel centerline.

When the Lewis number of hydrogen, Le_{H2}, was artificially set to unity (by equating the diffusivity of H_2 to the mixture thermal diffusivity), the flame moved farther away from the wall, as seen in Fig. 10d for the 15 bar case. This resulted in a dominant gas-phase conversion for the 15 bar case, as also shown in Fig. 13. The increase in Le_{H2} augmented substantially the laminar burning rates (e.g. for $p = 15$ bar and $T_o = 673$ K by a factor of 2.7 at $\varphi = 0.30$ and by a factor of 3.5 at $\varphi = 0.20$) due to the resulting rise of the hydrogen concentration at the beginning of the reaction zone [56], and at the same time led to higher amounts of hydrogen in the near-wall zone due to the reduced catalytic conversion. The latter could be seen from the 2-D hydrogen maps in Fig. 10c and d. Note that in Fig. 10d the H_2 radial flux through the flame had a peak value of 7.2 g/m^2 s, which was significantly higher than the corresponding peak values in Fig. 10a–c. This happened despite the fact that the radial hydrogen fluxes were, in the absence of gaseous reactions, considerably lower in Fig. 10d compared to Fig. 10a–c due to the ensuing slower catalytic conversion. The flame in Fig. 10d was strong enough to alter the fluid mechanical and catalytically-induced radial hydrogen fluxes and to further propagate to the channel center. It is finally noted that the introduction of flame propagation characteristics to assess gas-phase combustion behavior in catalytic channel-flow geometries had not received proper attention in the past.

In summary, the significant suppression of gaseous combustion at $p \geqslant 8$ bar and high preheats reflected the combined effects of the reduced laminar burning rates at these pressures and also of the high diffusivity of hydrogen that decreased the availability of fuel in the near-wall hot region. This picture was consistent with earlier hetero-/homogeneous combustion studies of methane [57], whereby gas-phase combustion intensified with rising pressure from 1 to 16 bar; methane was nearly diffusionally neutral ($Le_{CH4} \approx 1$) and its burning rates $\rho_o S_L$ increased with rising pressure as $p^{0.5}$. It is further noted that the geometrical confinement also affected the gaseous combustion behavior at high pressures: for the same inlet mass flux $\dot{m}$, smaller hydraulic diameter channels led to increased radial hydrogen fluxes towards the flame. This was a main reason that, for the wider channel used in the experiments, significant gas-phase combustion suppression was only observed at $p \geqslant 12$ bar (see Figs. 4 and 6).

The lower mass flux cases ($\dot{m} = 1.1$ kg/m^2 s, Fig. 9b) exhibited qualitatively the same behavior as the higher mass flux cases in Fig. 9a at $p = 1$ bar and $p \geqslant 8$ bar, when the reactor lengths in Fig. 9a and b were scaled to the corresponding mass flux ratio. For $p \geqslant 8$ bar the integrated G rate amounted to ~15% of the total integrated hydrogen conversion. At the intermediate pressures of 2 and 3.5 bar (where larger G rates were predicted for the higher max flux conditions in Fig. 9a), no plots have been given in

Fig. 9b since the resulting lower inflow velocities led to flames anchored directly at $x = 0$ such that a pure gas-phase microreactor was established. This behavior would have led to flame flashback in a practical burner.

For non-preheated mixtures (T_{IN} = 293 K) gas-phase conversion was minimal for the gas-turbine mass flux of $\dot{m} = 42.4$ kg/m^2 s and T_w = 1350 K. Plots similar to Fig. 9a indicated that the integrated G conversion amounted to less than 4% of the total hydrogen conversion for all pressures, despite the fact that homogeneous ignition occurred within the first 10 mm reactor length. The reason was the further reduced mass burning rates at T_{IN} = 293 K that could not accommodate the imposed radial hydrogen fluxes, as explained previously. For the microreactor mass flux $\dot{m} = 1.1$ kg/m^2 s and for T_{IN} = 293 K, the integrated G conversions were again minimal (less than 5% of the total integrated G conversions) for all pressures, except for p = 3.5 bar whereby the flame anchored at $x = 0$.

Finally, it is noted that the hetero-/homogeneous radical coupling had no appreciable impact on the aforementioned flame behavior. It may have been thought that as the flame was pushed against the wall at higher pressures, loss of radicals to the catalyst surface would have led to a stronger suppression of gaseous combustion. However, for the high wall and preheat temperatures in Figs. 9 and 10, computations with and without the inclusion of radical adsorption and desorption reactions (OH, O and H) gave practically the same results in terms of G conversion at all pressures.

4.3. Impact of preheat and confinement on gaseous combustion

The observed significant suppression of gaseous combustion at certain pressures had a significant impact on the reactor thermal management. In practical reactors the wall temperature was not uniform but locally varying as a result of the complex interplay between heat generation, heat redistribution mechanisms (heat conduction in the solid wall and in-channel surface radiation exchange), and external heat losses [58]. Under such conditions, it has been shown [31,34] that the presence of the near-wall gaseous combustion zone reduced appreciably the superadiabatic surface temperatures, which were in turn driven by the catalytic conversion of the low Lewis number hydrogen fuel. This was because the gaseous reaction zone shielded the catalyst from the hydrogen-rich channel core and thus reduced the catalytic conversion (see for example the 3.5 bar case in Fig. 10b and the corresponding C conversion rate in Fig. 9a). In this respect, the findings of the previous section (Figs. 9 and 10) suggested caution when combusting hydrogen or hydrogen-rich fuels in catalytic reactors either at atmospheric pressure or at elevated pressures $p \geqslant 8$ bar, since the moderating effect of gaseous combustion on the reactor wall temperature can be greatly reduced. The operating conditions under which gas-phase chemistry became important in catalytic systems was key input not only for practical reactor design but also for fundamental investigations of heterogeneous combustion of hydrogen (or hydrogen-rich fuels). For the latter studies, in particular, it was essential to recognize when gas-phase chemistry should be included in the simulations so as to avoid falsification of the modeled catalytic processes.

Detailed parametric numerical studies have been performed by varying the mixture preheat, the wall temperature and the channel geometrical confinement (size and type), for two different mass fluxes and for an H_2/air mixture with φ = 0.30. Channel lengths sufficient to ensure hydrogen conversions at least 99.5% at the outlet have been used in all cases. Figure 14 provides the percentage contribution of the gaseous pathway to the total (catalytic and

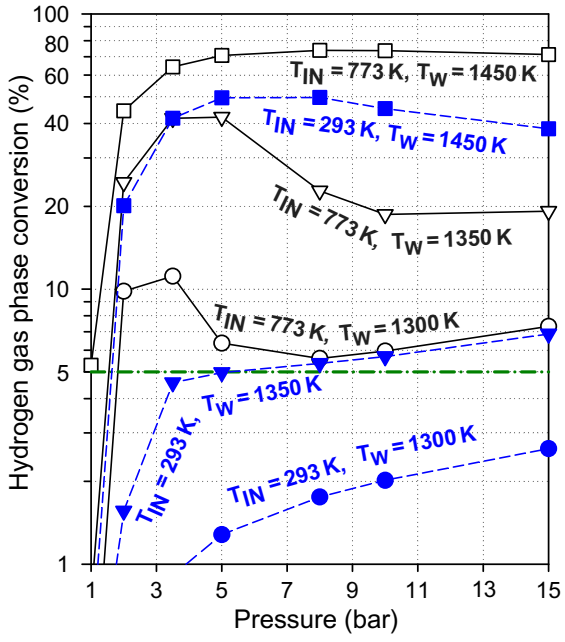

Fig. 14. Computed hydrogen gaseous conversion (as a percentage of the total conversion) in a tubular catalytic channel with d = 1 mm, for a φ = 0.30 H_2/air mixture, three wall temperatures, two inlet temperatures, and a constant mass flux $\dot{m} = 42.4$ kg/m^2 s.

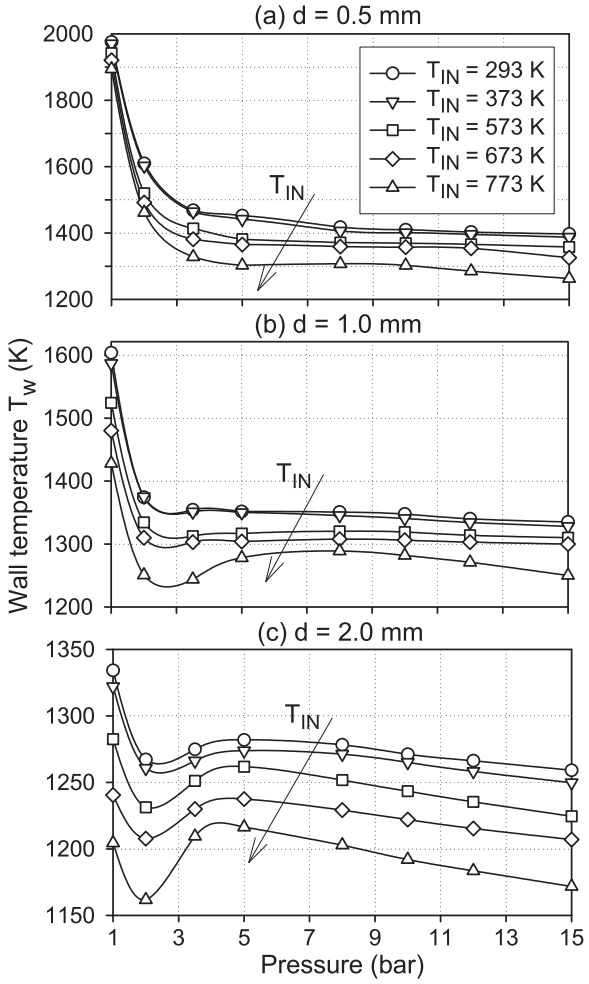

Fig. 15. Computed threshold wall temperatures, T_w, corresponding to 5% gaseous hydrogen conversion as a function of pressure for a φ = 0.30 H_2/air mixture at five different preheats and three catalytic channel diameters: (a) d = 0.5 mm, (b) d = 1.0 mm, and (c) d = 2.0 mm. The mass flux is for all cases $\dot{m} = 42.4$ kg/m^2 s.

gaseous) hydrogen conversion as a function of pressure for a tubular channel with diameter $d = 1$ mm, three different wall temperatures, two different preheats, and the gas-turbine-relevant mass flux $\dot{m} = 42.4$ kg/m^2 s. The operating conditions for which gas-phase chemistry amounted to 5% of the total (catalytic and gaseous) hydrogen conversion have subsequently been delineated. To accurately determine these limiting envelopes, successive simulations of the type shown in Fig. 14 were performed by increasing the wall temperature at increments as fine as 5 K, while keeping all other parameters constant. Threshold wall temperatures corresponding to 5% gaseous hydrogen conversion are plotted in Fig. 15 as a function of pressure for five different mixture preheats, three channel diameters ($d = 0.5$, 1.0 and 2.0 mm) and a constant mass flux $\dot{m} = 42.4$ kg/m^2 s. For the higher pressure range $p \geqslant 8$ bar, the threshold wall temperature required for achieving 5% gaseous conversion either remained constant or dropped with rising pressure. This was not inconsistent with the suppression of gaseous combustion at higher pressures reported in the previous section, since the 5% gaseous conversion limit was low enough such that the controlling factor was the ignition and not the propagation characteristics.

For typical channels in practical honeycomb reactors with $d = 1$ mm, the limiting wall temperatures for 5% gaseous conversion at $p > 2$ bar were $T_w \leqslant 1354$ K when $T_{IN} = 293$ K and $T_w \leqslant 1290$ K when $T_{IN} = 773$ K. Such wall temperatures were tolerable by reactor materials and catalysts, suggesting that at elevated pressure operation the gaseous pathway may not be ignored in practical honeycomb reactors having individual channel diameters $d = 1$ mm (corresponding to structures with ~400 cpsi, cells per square inch). At atmospheric pressure and for $d = 1$ mm, higher wall temperatures in the range 1428–1604 K were required to reach the 5% conversion threshold. As the channel diameter increased, the limiting wall temperatures dropped (see Fig. 15) as a result of the decreasing surface-to-volume ratio, which in turn promoted the volumetric gaseous combustion against the surface catalytic conversion. In particular, the limiting wall temperatures for $d = 2$ mm were in the range $1162 \text{ K} \leqslant T_w \leqslant 1334$ K (Fig. 15c), suggesting that for practical catalytic reactors using such channel geometries (for example, honeycomb structures having ~100 cpsi) gaseous combustion was not likely to be avoided at all pressures.

Threshold wall temperatures for the low flow rate $\dot{m} = 1.1$ kg/m^2 s relevant to microreactors are provided in Fig. 16 at two preheats and three channel diameters, and further compared against the corresponding higher mass flux cases in Fig. 15. For $p \geqslant 2$ bar, the computed wall temperatures for the lower mass flux cases were modestly lower compared to their higher mass flux counterparts (by as much as 40 K for $d = 0.5$ mm, 18 K for $d = 1.0$ mm, and 6 K for $d = 2$ mm). At atmospheric pressure the differences were up to 230 K for the smaller diameter channel $d = 0.5$ mm and dropped to 42 K for $d = 1.0$ mm. This behavior was due to the very small G conversion at atmospheric pressure (see for example Fig. 9) and its resulting higher sensitivity on the particular value of the wall temperature. For the larger diameter case ($d = 2$ mm, Fig. 16c) the reduced impact of geometrical confinement led to threshold wall temperature differences between the high and low mass flux cases of less than 18 K for all pressures.

Finally, the type of confinement – cylindrical versus planar geometry – has been investigated in Fig. 17. Simulations are shown for two preheats and two geometrical confinements (0.5 mm and 1.0 mm) corresponding to the full height ($2b$) or diameter (d) of the channel. For pressures $p \geqslant 3.5$ bar the threshold wall temperature differences between the two geometries were less than 22 K for the higher preheat case $T_{IN} = 573$ K and less than 6 K for

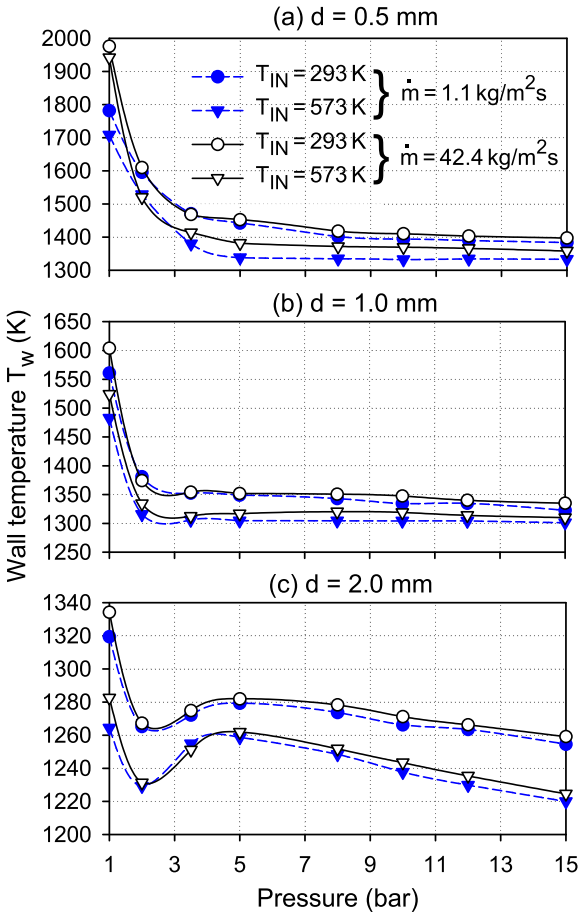

Fig. 16. Computed threshold wall temperatures, T_w, corresponding to 5% gaseous hydrogen conversion, as a function of pressure for a $\varphi = 0.30$ H_2/air mixture at two different preheats and two mass fluxes: $\dot{m} = 42.4$ kg/m^2 s (open symbols) and $\dot{m} = 1.1$ kg/m^2 s (filled symbols). Catalytic channel diameters: (a) $d = 0.5$ mm, (b) $d = 1.0$ mm, and (c) $d = 2.0$ mm.

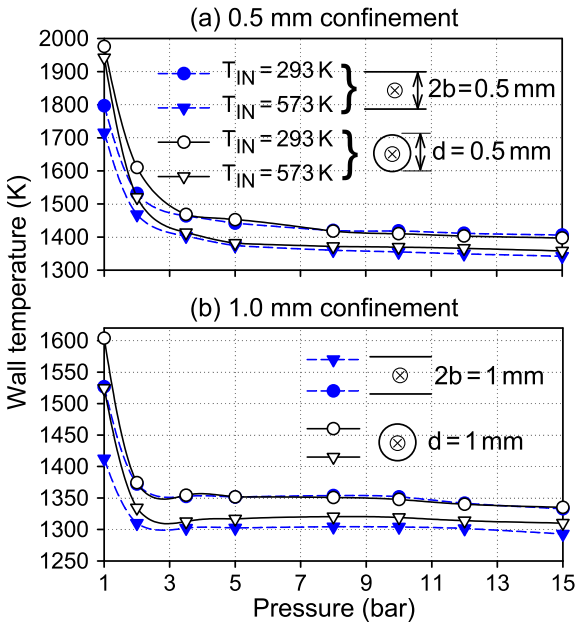

Fig. 17. Computed threshold wall temperatures, T_w, corresponding to 5% gaseous hydrogen conversion, as a function of pressure for a $\varphi = 0.30$ H_2/air mixture at two different preheats, two geometry types (tubular: open symbols, planar: filled symbols) and a constant mass flux $\dot{m} = 42.4$ kg/m^2 s. (a) 0.5 mm tubular channel diameter or planar channel full height, and (b) 1.0 mm tubular channel diameter or planar channel full height.

T_{IN} = 293 K. The corresponding differences were more pronounced at $p \leqslant 2$ bar, reaching up to 225 K at 1 bar. This was due to the weaker confinement for the plane channel geometry (the hydraulic diameter for a plane channel is twice the channel full height D_h = 4b, whereas for a cylindrical geometry $D_h = d$). This led to a smaller surface-to-volume ratio for the plane channel, which in turn favored gaseous combustion. The more pronounced impact at atmospheric pressure was exactly for the same reason described in Fig. 16, i.e. the higher sensitivity of gaseous combustion on the wall temperature at this pressure.

The graphs in Figs. 15–17 can be used for a first assessment whether gas-phase combustion is important in various applications. Wall temperatures can be monitored with thermocouples in gas turbine catalytic reactors, microreactors and laboratory reactors or can be predicted with simplified models. The resulting wall temperatures can then be compared to the threshold wall temperatures in Figs. 15–17.

5. Conclusions

The hetero-/homogeneous combustion of fuel-lean $H_2/O_2/N_2$ mixtures over Pt was investigated experimentally and numerically at pressures and preheats of up to 15 bar and 790 K, respectively, which were relevant to gas turbine applications. In situ 1-D spontaneous Raman measurements and planar LIF of the OH radical were applied in an optically accessible channel-flow rectangular catalytic reactor with a height of 7 mm in order to monitor the catalytic and gas-phase combustion processes, respectively. Simulations were carried out to assess the performance of hetero-/homogeneous kinetic schemes and to clarify the intricate pressure/temperature dependence of the hydrogen homogeneous kinetics and their coupling to transport. Additional simulations were performed in practical channels with geometrical confinements of 0.5–2 mm so as to evaluate the significance of gas-phase chemistry at different pressures, temperatures and mass throughputs. The following are the key conclusions of this study.

(1) The employed hetero-/homogeneous reaction schemes reproduced the LIF-measured onset of homogeneous ignition and the subsequent flame propagation in the catalytic channel, over the examined pressure, preheat and wall temperature ranges. Moreover, for the investigated conditions mass-transport limited catalytic conversion of hydrogen was attested by both Raman measurements and model predictions.

(2) Measurements and predictions in the optically accessible reactor indicated that even with modest preheats of 390 K, appreciable gaseous combustion could be sustained for pressures up to 10 bar, a range of interest for small-scale industrial turbines and also for microturbine-driven portable power generation systems. On the other hand, as pressure increased above 10 bar the preheat requirements for significant gas-phase conversion raised appreciably. For p = 15 bar (a pressure relevant for large gas turbines) even preheats up to 758 K, typical to full load operation, were not adequate to initiate significant gas-phase conversion.

(3) Simulations in practical geometrical confinements of 1 mm were performed for mass fluxes relevant to both large-scale gas turbines and microreactors. At such large confinements, gas-phase combustion was altogether suppressed at atmospheric pressure, wall temperatures as high as 1350 K and preheats up to 773 K. This was a result of the slower gaseous ignition chemistry in combination with the increased hydrogen catalytic consumption over the elongated gas-phase induction zone.

(4) While homogeneous ignition kinetics was crucial at atmospheric pressure, flame propagation characteristics played a key role for the establishment of flames at the higher pressure range. The decrease in laminar burning rates at $p \geqslant 8$ bar led to a push of the gaseous reaction zone close to the channel wall, to a subsequent leakage of hydrogen through the gaseous reaction zone, and finally to catalytic conversion of the escaped fuel at the wall. This process led to greatly reduced gaseous hydrogen conversion for $p \geqslant 8$ bar, suggesting care when designing gas turbine catalytic reactors for hydrogen and hydrogen-rich containing fuels. The reason was the beneficial impact of gaseous combustion in hydrogen-fueled catalytic reactors by moderating the catalytically-induced superadiabatic surface temperatures.

(5) For practical geometrical confinements of 1 mm and for large mass fluxes typical to large-scale gas turbines, vigorous gaseous combustion could be established for pressures between 2 and 5 bar, for preheats as high as 773 K and wall temperatures of 1350 K. Moreover, for lower mass fluxes relevant to microreactors the same trends as in the higher mass flux cases have been demonstrated for atmospheric pressure and for the high-end pressure range $p \geqslant 8$ bar. For intermediate pressures, gaseous combustion was accelerated in the microreactor leading eventually to flame flashback due to reduced inflow velocities.

(6) Parametric studies have delineated the threshold wall temperatures required for a 5% gas-phase hydrogen conversion, as a function of mixture preheat, pressure, geometrical confinement and mass throughput. It was shown that for a range of wall temperatures tolerable by most ceramic and metallic catalytic reactor materials ($T_w \leqslant 1350$ K), gaseous combustion could not be neglected for channel diameters $d \geqslant 1$ mm, pressures $p > 2$ bar, and preheats $T_{IN} \geqslant 293$ K. At p = 1 bar and for the previously mentioned operating conditions and geometrical confinements, the threshold wall temperatures were significantly higher, 1428 K $\leqslant T_w \leqslant$ 1604 K. For $d \geqslant 1$ mm the threshold wall temperatures were only modestly reduced at all pressures (by up to 42 K) when lowering the incoming mass flux by a factor of ~40. Finally, the type of geometrical confinement (tubular or plane channel) had a significant impact only at atmospheric pressure and large geometrical confinements (=0.5 mm).

Acknowledgments

We would like to acknowledge the help of Mr. Rene Kaufmann in the experiments and the support from the Swiss Commission of Technology and Innovation (KTI), the Swiss Competence Center of Energy and Mobility (CCEM), and the European Union via the Hydrogen IGCC project.

References

[1] S. Hoffmann, M. Bartlett, M. Finkenrath, A. Evulet, T.P. Ursin, Performance and cost analysis of advanced gas turbine cycles with precombustion CO_2 capture, ASME GT2008-51027, 2008.
[2] D. Winkler, P. Mueller, S. Reimer, T. Griffin, A. Burdet, J. Mantzaras, Y. Ghermay, Improvement of gas turbine combustion reactivity under flue gas recirculation condition with in situ hydrogen addition, ASME GT2009-59182, 2009.
[3] C. Appel, J. Mantzaras, R. Schaeren, R. Bombach, A. Inauen, N. Tylli, M. Wolf, T. Griffin, D. Winkler, R. Carroni, Proc. Combust. Inst. 30 (2005) 2509–2517.
[4] D.G. Norton, E.D. Wetzel, D.G. Vlachos, Ind. Eng. Chem. Res. 43 (2004) 4833–4840.
[5] V. Seshadri, N.S. Kaisare, Combust. Flame 157 (2010) 2051–2062.
[6] G.D. Stefanidis, D.G. Vlachos, N.S. Kaisare, M. Maestri, AIChE J. 55 (2009) 180–191.
[7] R. Horn, K.A. Williams, N.J. Degenstein, A. Bitsch-Larsen, D.D. Nogare, S.A. Tupy, L.D. Schmidt, J. Catal. 249 (2007) 380–393.

[8] W.M. Budzianowski, Int. J. Hydrogen Energy 35 (2010) 7454–7469.
[9] M. Hartmann, L. Maier, H.D. Minh, O. Deutschmann, Combust. Flame 157 (2010) 1771–1782.
[10] N. Hotz, M.J. Stutz, S. Loher, W.J. Stark, D. Poulikakos, Appl. Catal. B – Environ. 73 (2007) 336–344.
[11] C.M. Balonek, J.L. Colby, L.D. Schmidt, AIChE J. 56 (2010) 979–988.
[12] R. Carroni, T. Griffin, Catal. Today 155 (2010) 2–12.
[13] G. Pizza, C.E. Frouzakis, J. Mantzaras, A.G. Tomboulides, K. Boulouchos, Combust. Flame 155 (2008) 2–20.
[14] G. Pizza, C.E. Frouzakis, J. Mantzaras, A.G. Tomboulides, K. Boulouchos, J. Fluid Mech. 658 (2010) 463–491.
[15] K. Maruta, T. Kataoka, N.I. Kim, S. Minaev, R. Fursenko, Proc. Combust. Inst. 30 (2004) 2429–2436.
[16] C.J. Evans, D.C. Kyritsis, Proc. Combust. Inst. 32 (2009) 3107–3114.
[17] G. Pizza, J. Mantzaras, C.E. Frouzakis, A.G. Tomboulides, K. Boulouchos, Proc. Combust. Inst. 32 (2009) 3051–3058.
[18] G. Pizza, J. Mantzaras, C.E. Frouzakis, Catal. Today 155 (2010) 123–130.
[19] O. Deutschmann, R. Schmidt, F. Behrendt, J. Warnatz, Proc. Combust. Inst. 26 (1996) 1747–1754.
[20] M. Rinnemo, O. Deutschmann, F. Behrendt, B. Kasemo, Combust. Flame 111 (1997) 312–326.
[21] M. Maestri, A. Beretta, T. Faravelli, G. Groppi, E. Tronconi, D.G. Vlachos, Chem. Eng. Sci. 63 (2008) 2657–2669.
[22] B. Hellsing, B. Kasemo, V.P. Zhdanov, J. Catal. 132 (1991) 210–228.
[23] O. Deutschmann, L.I. Maier, U. Riedel, A.H. Stroemman, R.W. Dibble, Catal. Today 59 (2000) 141–150.
[24] J. Ludwig, D.G. Vlachos, J. Chem. Phys. 128 (2008) 154708.
[25] J.D. Grunwaldt, B. Kimmerle, A. Baiker, P. Boye, C.G. Schroer, P. Glatzel, C.N. Borca, F. Beckmann, Catal. Today 145 (2009) 267–278.
[26] J. Li, Z. Zhao, A. Kazakov, F.L. Dryer, Int. J. Chem. Kinet. 36 (2004) 566–575.
[27] M.P. Burke, F.L. Dryer, Y. Ju, Proc. Combust. Inst. 33 (2010), doi:10.1016/j.proci.2010.05.021.
[28] P. Saxena, F.A. Williams, Combust. Flame 145 (2006) 316–323.
[29] J. Li, Z.W. Zhao, A. Kazakov, M. Chaos, F.L. Dryer, J.J. Scire, Int. J. Chem. Kinet. 39 (2007) 109–136.
[30] P.A. Bui, D.G. Vlachos, P.R. Westmoreland, Proc. Combust. Inst. 26 (1996) 1763–1770.
[31] C. Appel, J. Mantzaras, R. Schaeren, R. Bombach, A. Inauen, B. Kaeppeli, B. Hemmerling, A. Stampanoni, Combust. Flame 128 (2002) 340–368.
[32] M. Maestri, A. Beretta, T. Faravelli, G. Groppi, E. Tronconi, Chem. Eng. Sci. 62 (2007) 4992–4997.
[33] J. Mantzaras, R. Bombach, R. Schaeren, Proc. Combust. Inst. 32 (2009) 1937–1945.
[34] Y. Ghermay, J. Mantzaras, R. Bombach, Combust. Flame 157 (2010) 1942–1958.
[35] J. Mantzaras, Combust. Sci. Technol. 180 (2008) 1137–1168.
[36] G. Groppi, A. Belloli, E. Tronconi, P. Forzatti, Catal. Today 29 (1996) 403–407.
[37] A. Scarpa, P.S. Barbato, G. Landi, R. Pirone, G. Russo, Chem. Eng. J. 154 (2009) 315–324.
[38] S. Specchia, L.D. Vella, S. Burelli, G. Saracco, V. Specchia, ChemPhysChem 10 (2009) 783–786.
[39] S. Karagiannidis, J. Mantzaras, R. Bombach, S. Schenker, K. Boulouchos, Proc. Combust. Inst. 32 (2009) 1947–1955.
[40] M. Reinke, Mantzaras, R. Bombach, S. Schenker, N. Tylli, K. Boulouchos, Combust. Sci. Technol. 179 (2007) 553–600.
[41] M. Reinke, J. Mantzaras, R. Schaeren, R. Bombach, A. Inauen, S. Schenker, Combust. Flame 136 (2004) 217–240.
[42] W.C. Pfefferle, L.D. Pfefferle, Prog. Energy Combust. Sci. 12 (1986) 25–41.
[43] R.J. Kee, G. Dixon-Lewis, J. Warnatz, M.E. Coltrin, J.A. Miller, A Fortran computer code package for the evaluation of gas-phase multicomponent transport properties, Report No. SAND86-8246, 1996.
[44] J. Warnatz, M.D. Allendorf, R.J. Kee, M.E. Coltrin, Combust. Flame 96 (1994) 393–406.
[45] R.J. Kee, F.M. Rupley, J.A. Miller, Chemkin II: a Fortran chemical kinetics package for the analysis of gas-phase chemical kinetics, Report No. SAND89-8009B, 1996.
[46] M.E. Coltrin, R.J. Kee, F.M. Rupley, Surface Chemkin: a Fortran package for analyzing heterogeneous chemical kinetics at the solid surface–gas phase interface, Report No. SAND90-8003C, 1996.
[47] C. Appel, J. Mantzaras, R. Schaeren, R. Bombach, A. Inauen, Combust. Flame 140 (2005) 70–92.
[48] B. Schneider, S. Karagiannidis, M. Bruderer, D. Dyntar, C. Zwyssig, Q. Guangchun, M. Diener, K. Boulouchos, R.S. Abhari, L. Guzzella, J.W. Kolar, Ultra-high-energy-density converter for portable power, Power-MEMS 2005, Tokyo, Japan, November 28–30, 2005.
[49] J. Mantzaras, C. Appel, Combust. Flame 130 (2002) 336–351.
[50] A.E. Lutz, R.J. Kee, J.A. Miller, SENKIN: a Fortran program for predicting homogeneous gas phase chemical kinetics with sensitivity analysis, Report No. SAND87-8248, 1996.
[51] I. Glassman, Combustion, Academic Press, London, 1996. p. 67.
[52] R. Carroni, T. Griffin, J. Mantzaras, M. Reinke, Catal. Today 83 (2003) 157–170.
[53] J. Mantzaras, P. Benz, Combust. Flame 119 (1999) 455–472.
[54] F.M. Rupley, R.J. Kee, J.A. Miller, Premix: a Fortran program for modeling steady laminar one-dimensional premixed flames, Report No. SAND85-8240, 1995.
[55] C.K. Law, G.I. Sivashinsky, Combust. Sci. Technol. 29 (1982) 277–286.
[56] F.A. Williams, Combustion Theory, Benjamin/Cummings, Menlo Park, CA, 1985. p. 164.
[57] M. Reinke, J. Mantzaras, R. Bombach, S. Schenker, A. Inauen, Combust. Flame 141 (2005) 448–468.
[58] S. Karagiannidis, J. Mantzaras, G. Jackson, K. Boulouchos, Proc. Combust. Inst. 31 (2007) 3309–3317.